RESEARCH ARTICLE

Discovery and Clinical Proof-of-Concept of RLY-2608, a First-in-Class Mutant-Selective Allosteric PI3Kα Inhibitor That Decouples Antitumor Activity from Hyperinsulinemia

Andreas Varkaris[1], Ermira Pazolli[2], Hakan Gunaydin[2], Qi Wang[3], Levi Pierce[2], Alessandro A. Boezio[2], Artemisa Bulku[2], Lucian DiPietro[2], Cary Fridrich[2], Adam Frost[4,5,6], Fabrizio Giordanetto[3], Erika P. Hamilton[7], Katherine Harris[8], Michael Holliday[2], Tamieka L. Hunter[2], Amanda Iskandar[2], Yongli Ji[9], Alexandre Larivée[10], Jonathan R. LaRochelle[2], André Lescarbeau[2], Fabien Llambi[2], Brenda Lormil[1], Mary M. Mader[2], Brenton G. Mar[2], Iain Martin[2], Thomas H. McLean[2], Klaus Michelsen[2], Yakov Pechersky[3], Erika Puente-Poushnejad[2], Kevin Raynor[2], Dipali Rogala[2], Ramin Samadani[2], Alison M. Schram[11], Kelley Shortsleeves[2], Sweta Swaminathan[2], Shahein Tajmir[12], Gege Tan[2], Yong Tang[2], Roberto Valverde[2], Bryan Wehrenberg[2], Jeremy Wilbur[2], Bret R. Williams[2], Hongtao Zeng[2], Hanmo Zhang[2], W. Patrick Walters[1], Beni B. Wolf[2], David E. Shaw[3,13], Donald A. Bergstrom[2], James Watters[2], James S. Fraser[6,14], Pascal D. Fortin[2], and D. Randal Kipp[2]

ABSTRACT *PIK3CA* (PI3Kα) is a lipid kinase commonly mutated in cancer, including ~40% of hormone receptor–positive breast cancer. The most frequently observed mutants occur in the kinase and helical domains. Orthosteric PI3Kα inhibitors suffer from poor selectivity leading to undesirable side effects, most prominently hyperglycemia due to inhibition of wild-type (WT) PI3Kα. Here, we used molecular dynamics simulations and cryo-electron microscopy to identify an allosteric network that provides an explanation for how mutations favor PI3Kα activation. A DNA-encoded library screen leveraging electron microscopy-optimized constructs, differential enrichment, and an orthosteric-blocking compound led to the identification of RLY-2608, a first-in-class allosteric mutant-selective inhibitor of PI3Kα. RLY-2608 inhibited tumor growth in *PIK3CA*-mutant xenograft models with minimal impact on insulin, a marker of dysregulated glucose homeostasis. RLY-2608 elicited objective tumor responses in two patients diagnosed with advanced hormone receptor–positive breast cancer with kinase or helical domain *PIK3CA* mutations, with no observed WT PI3Kα-related toxicities.

SIGNIFICANCE: Treatments for *PIK3CA*-mutant cancers are limited by toxicities associated with the inhibition of WT PI3Kα. Molecular dynamics, cryo-electron microscopy, and DNA-encoded libraries were used to develop RLY-2608, a first-in-class inhibitor that demonstrates mutant selectivity in patients. This marks the advance of clinical mutant-selective inhibition that overcomes limitations of orthosteric PI3Kα inhibitors.

See related article by Varkaris et al.

INTRODUCTION

Phosphoinositide 3-kinases (PI3K) catalyze the conversion of phosphatidylinositol bisphosphate $PI(4,5)P_2$ to phosphatidylinositol-3,4,5-triphosphate, or PIP_3 (1). The production of these phospholipids can anchor proteins involved in signal transduction cascades that influence a wide range of cellular processes, including growth and survival (2). Accordingly, in PI3Ks, the enzymatic activity of the catalytic subunit is tightly controlled by a regulatory subunit in a dimeric assembly (3). Recent hydrogen–deuterium exchange (4) and cryo-electron microscopy (cryoEM) (5) studies can be synthesized with classic biochemical studies to suggest an overall model of PI3K activation. Many inputs, including phosphopeptide binding to the regulatory subunit (6) and membrane localization (4), contribute to biasing the conformational equilibrium to loosen the interactions between the regulatory and catalytic subunits, activating the lipid kinase (7).

This conformational regulation is presumed to be disrupted in cancer where mutations to PI3Ks are common (8). One PI3K isoform, *PIK3CA*, is the most recurrently mutated kinase in cancer, occurring in 14% of all solid tumors (8), and up to 40% in hormone receptor (HR) positive, human epidermal growth factor 2 (HER2)-negative breast cancer. Encoding the p110α catalytic subunit of phosphoinositide 3-kinase alpha (PI3Kα), *PIK3CA* is commonly mutated at "hotspot" activating mutations occurring both in the kinase (H1047R) and helical (E542K, E545K) domains (9). Extensive clinical development of orthosteric inhibitors of PI3Kα led to the approval of alpelisib (in combination with the selective estrogen receptor degrader, fulvestrant) for the treatment of patients with advanced HR^+ $HER2^-$ breast cancer with prior endocrine therapy. Unfortunately, orthosteric inhibitors such as alpelisib are not mutant-selective and inhibit WT PI3Kα, which plays a critical role in cellular glucose uptake and insulin response (10), leading to dose-limiting toxicity such as hyperglycemia and hyperinsulinemia (11). The development of mutant-selective PI3Kα inhibitors could potentially overcome these limitations.

Structures of H1047R PI3Kα obtained by X-ray crystallography (12) and cryoEM (13, 14) have linked the mutation to disruption of the conformation of the C-terminal tail of p110α. Although the conformation in the H1047R X-ray structure is stabilized by crystal contacts involving tail residues 1050–1062 (13), which are not resolved in the electron microscopy (EM) data, this perturbed conformation may cooperate with the additional

[1]Mass General Cancer Center and Department of Medicine, Harvard Medical School, Boston, Massachusetts. [2]Relay Therapeutics, Inc., Cambridge, Massachusetts. [3]D. E. Shaw Research, New York, New York. [4]Altos Labs, Institute of Science, San Francisco, California. [5]Department of Biochemistry and Biophysics, University of California San Francisco, San Francisco, California. [6]California Institute of Quantitative Biosciences (QB3), University of California San Francisco, San Francisco, California. [7]Sarah Cannon Research Institute/Tennessee Oncology, Nashville, Tennessee. [8]MGH/Mass General Cancer Center at Danvers, Danvers, Massachusetts. [9]Hematology/Oncology, Exeter Hospital, Exeter, New Hampshire. [10]Paraza Pharma, Inc. Montreal, Canada. [11]Department of Medicine, Memorial Sloan Kettering Cancer Center, New York, New York. [12]MGH Radiology, Harvard Medical School, Boston, Massachusetts. [13]Department of Biochemistry and Molecular Biophysics, Columbia University, New York, New York. [14]Department of Bioengineering and Therapeutic Sciences, University of California San Francisco, San Francisco, California.

A.A. Boezio, A. Bulku, M.M. Mader, K. Michelsen, Y. Pechersky, Y. Tang, B.R. Williams, and H. Zhang conducted this research while employed by the institutions noted in their respective affiliations.

Corresponding Authors: D. Randal Kipp, Relay Therapeutics, Inc., 399 Binney Street, Cambridge, MA 02139. E-mail: rkipp@relaytx.com; and Pascal D. Fortin, Relay Therapeutics, Inc., 399 Binney Street, Cambridge, MA 02139. E-mail: pfortin@relaytx.com

Cancer Discov 2024;14:1–18

doi: 10.1158/2159-8290.CD-23-0944

positive charge on 1047R to promote interactions with the membrane (12). The lack of density for the tail in the EM analysis suggested a more dominant role for reducing the inhibitory effect of the PI3Kα regulatory subunit, p85α, in the activation by H1047R. Moreover, the cryoEM structures of helical and H1047R mutants reveal no major changes that propagate to the active site (12, 13), where the phosphate from ATP is transferred to the lipid, suggesting that the mechanism for activation is the result of conformational regulation rather than a perturbed active site.

These structural data illustrate the great difficulty of developing both isoform- and mutant-selective inhibitors. The PI3K active site is well conserved across isoforms (α, β, γ, and δ), and orthosteric pan-PI3K inhibitors have been limited in use by toxicity (15–17). Mutant selectivity is even more challenging because the p110α active site is not mutated or conformationally perturbed in the most prevalent mutants. Achieving selectivity is especially important because WT PI3Kα plays a critical role in cellular glucose uptake and insulin response (10). Current isoform-selective PI3Kα inhibitors lead to dose-limiting hyperglycemia and consequent hyperinsulinemia (11) among other side effects (18) due to their potency against the WT protein. The limited efficacy of current ATP binding site targeting agents has motivated significant research aimed at the discovery of mutant-selective PI3Kα inhibitors across academic and industrial institutions.

Here, we have analyzed the conformational differences between mutant and WT PI3Kα using unbiased molecular dynamics (MD) simulations based on a new cryoEM structure of apo PI3Kα that we determined. This analysis pointed to the existence of a key allosteric network, raising the possibility that PI3Kα mutants can be inhibited selectively over the WT based on differential conformational dynamics. Identifying mutant-specific chemical matter from a DNA-encoded library (DEL) screen enabled the development of potent inhibitors that are isoform- and mutant-selective. These molecules result in tumor regression *in vivo*, with negligible increase in insulin, a marker of hyperglycemia. These preclinical findings are validated in the clinic with two case studies presented here from an ongoing first-in-human study of RLY-2608. Among these cases, which include a patient with HR-positive, *PIK3CA* H1047R-metastatic breast cancer and a patient with HR-positive, *PIK3CA* E542K-metastatic breast cancer, partial responses were observed in the absence of PI3Kα WT-related toxicities.

RESULTS

CryoEM and MD Simulations Reveal Dynamic Differences between WT and H1047R PI3Kα

We generated a 2.7 Å-resolution cryoEM reconstruction of the full-length WT p85α:p110α heterodimer in the apo state (Fig. 1A). The overall architecture of the enzyme and relationship between the catalytic and regulatory subunits is similar to prior structures, including those with active site inhibitors or nanobodies bound (5, 14). All domains of the p110α subunit were sufficiently well resolved to model, as were the iSH2 and nSH2 domains of the p85α subunit. No clear density was observed for the SH3, BH, or cSH2 domains of p85α. The density map had a clear definition of the C-terminal tail near H1047, extending to residue T1053, and much of the kinase activation loop (Fig. 1A). Although a short segment of the activation loop remains poorly resolved (residues 945–948), the resolved density indicates an interaction between the activation loop and p85α iSH2 residue Arg577 (Fig. 1A), providing a potential connection between the regulatory subunit and the activation mechanism of the kinase domain.

To investigate the impact of the H1047R mutation on the regulation of PI3Kα, we carried out long-timescale MD simulations initiated from a model based on our cryoEM structure of apo PI3Kα. We performed multiple independent 10-μs simulations on WT and H1047R PI3Kα systems. To prepare the H1047R simulations, we mutated the residue *in silico*, but otherwise used the WT cryoEM model. In WT simulations, the conformation of the tail remains stable and consistent with prior structures: H1047 and W1051 remain associated with F954 of the kinase domain C-lobe throughout the entirety of each simulation (Fig. 1B). In contrast, for simulations of H1047R, both R1047 and W1051 show increased conformational dynamics and begin to disengage from the rest of p110α (Fig. 1B). However, the conformations observed in the H1047R MD simulations are not as dramatic as the disengaged conformation observed in the X-ray structure {PDB 3HHM}, (which extends to residue 1062 and is stabilized by crystal contacts) or the recent cryoEM structure of H1047R {PDB 8GUB} (which extends only to residue G1050). The simulation results suggest that the fully disengaged tail conformation seen in the crystal structure may happen at a timescale substantially longer than 10 μs or may be promoted by crystal contacts.

To test these possibilities, we initiated simulations from the crystal structure conformation of H1047R PI3Kα, where the fully disengaged tail is stabilized by significant crystal lattice contacts, and for the H1047R kinase domain alone (without p85α). Even when freed from the crystalline environment, the H1047R simulations initiated from the crystal structure demonstrate a dramatically perturbed conformational ensemble relative to WT PI3Kα (Fig. 1B). Tail residues, including R1047 and W1051, are exposed, and several regions of the protein shift conformation.

For example, we observe that the activation loop is slightly more disordered in the mutant than in WT (Supplementary Fig. S1A and S1B). This led us to hypothesize that there might be allosteric communication between these two distant structural elements. In simulations of the mutant, our analysis showed that residues F954 of the C-lobe and D915 of the HRD motif, located in between the tail and the activation loop, are perturbed away from the positions observed in WT and sample more diverse conformations (Fig. 1C). This analysis suggests these residues may play a key role in the allosteric network connecting the site of mutation to the activation loop.

We next initiated simulations of the H1047R kinase domain without the p85α regulatory subunit present. These 100-μs simulations begin with a tail-buried conformation based on our WT cryoEM structure. In all 5 replicates, the tail, including R1047 and W1051, becomes exposed and populates an ensemble similar to the disengaged states observed in the H1047R crystal structure (Fig. 1B). Similar changes are also observed throughout the allosteric network connecting the tail conformation (Supplementary Fig. S2A) to the HRD motif and the activation loop (Supplementary Fig. S2B), which is even more disordered at the longer timescales simulated here than in the shorter simulations described above. We did not observe any increased

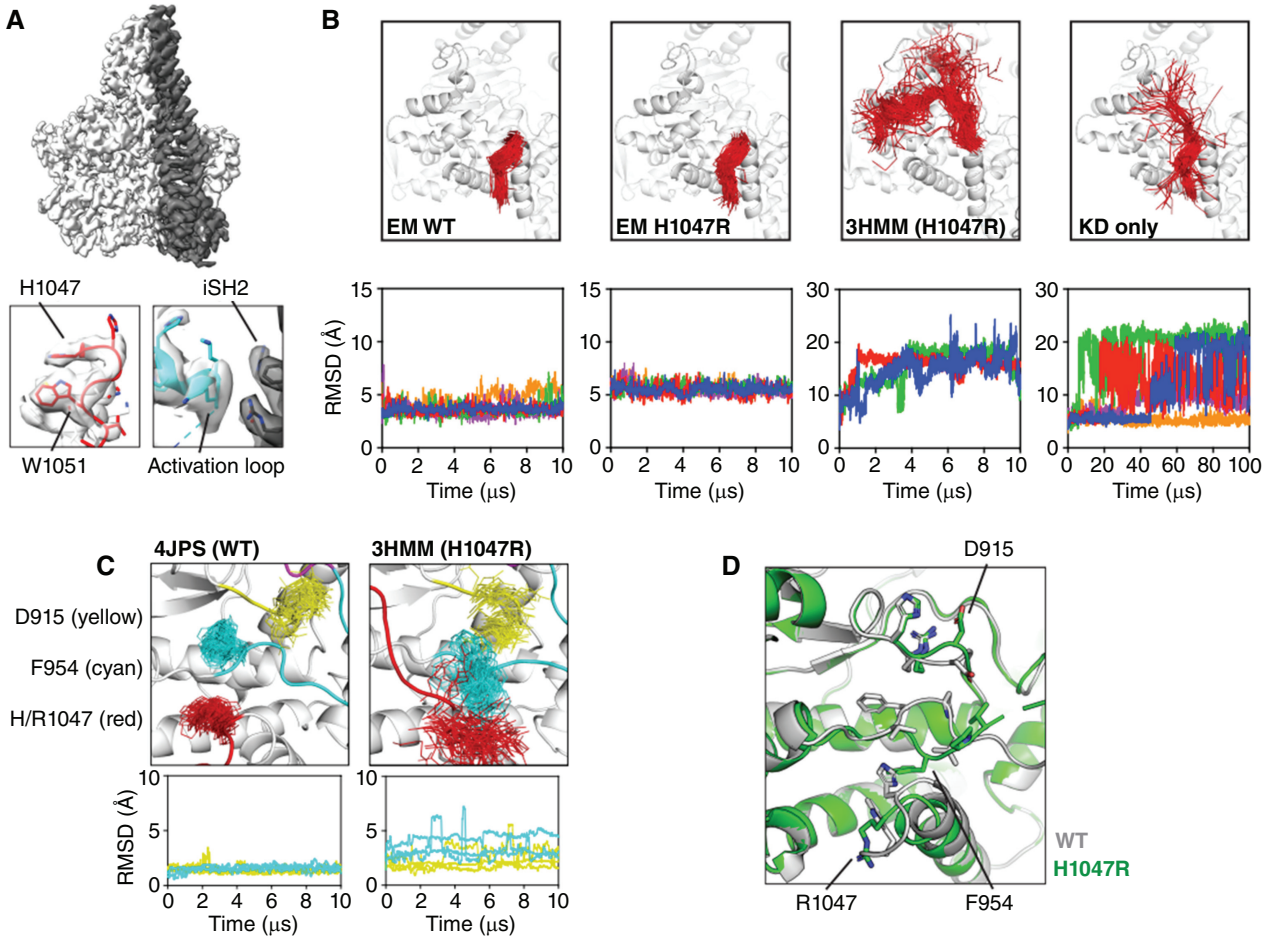

Figure 1. **A,** CryoEM density map for PI3Kα, with p110α shaded white and p85α shaded gray. Inset views of the modeled structure and density map for the C-terminal tail (red) and activation loop (cyan). **B,** States sampled by WT (EM), H1047R (EM), and H1047R (PDB 3HMM) throughout a single 10-μs simulation, with the C-terminal tail (residues 1047–1062) in red. Tail RMSD values throughout three to five 10 μs replicates, colored independently, are plotted below). States sampled by kinase domain (KD) throughout 5 × 100 μs simulations. **C,** States sampled by WT (top left) or H1047R (top right) throughout a single 10-μs simulation. Residues 915 (yellow), 954 (cyan), and 1047 (red) are depicted as sticks. RMSD values throughout three 10-μs replicates are plotted below for residues 915 (yellow) and 954 (cyan). **D,** Overlayed, isomorphous crystal structures of PI3Kα WT (gray) and H1047R (green). RMSD, root mean square deviation.

conformational dynamics in equivalent simulations totaling 500 μs for the WT kinase domain without p85α present, and the activation loop is more ordered than in the H1047R simulation (Supplementary Fig. S1B). These simulations overcome the restrictions of the crystal environment from the X-ray structure of H1047R (12) to provide an unbiased view of how tail conformational dynamics are perturbed by mutation.

To further address the connection between a disengaged tail conformation and kinase activation, we solved structures of PI3Kα WT and H1047R in an alternative crystal system that enabled isomorphous comparisons (Fig. 1D). For the WT, we observed density for the tail consistent with the buried conformation, extending to residue W1051. In contrast, for H1047R, we observed density consistent with a disengaged conformation extending to residue R1047. These structures are consistent with the simulations, indicating that the F954 loop rotates toward the C-terminal tail in H1047R, but not WT contexts. F954 fills the space occupied by H1047 in the WT structure. Relative to the WT structure, the mutant also exhibits a considerable shift in the C-terminal end of the activation loop, comprising residues 949–955. This observation is consistent with the idea that the connection to the p85α regulatory subunit is weakened in H1047R. Collectively, these analyses suggest that H1047R populates a significantly perturbed conformational landscape relative to WT, with the disengaged tail conformation favored. This expanded ensemble is observed in our simulations initiated from disengaged conformation and from the isolated H1047R kinase domain initiated from the buried conformation. Although the specific conformation observed in the original H1047R crystal structure is biased by crystal contacts, it provides a useful relatively low-energy starting point for simulations that explore the expanded ensemble of the disengaged tail. In addition, our new crystal form indicates that the tail is quite disordered for the mutant relative to WT. Furthermore, the structural and simulation data suggest that the exchange from the buried to the disengaged conformation is much slower than the simulation timescale when the p85α subunit is bound, even for H1047R.

Our cryoEM, MD, and X-ray results, together with the recently published HDX data (4), support the model proposed

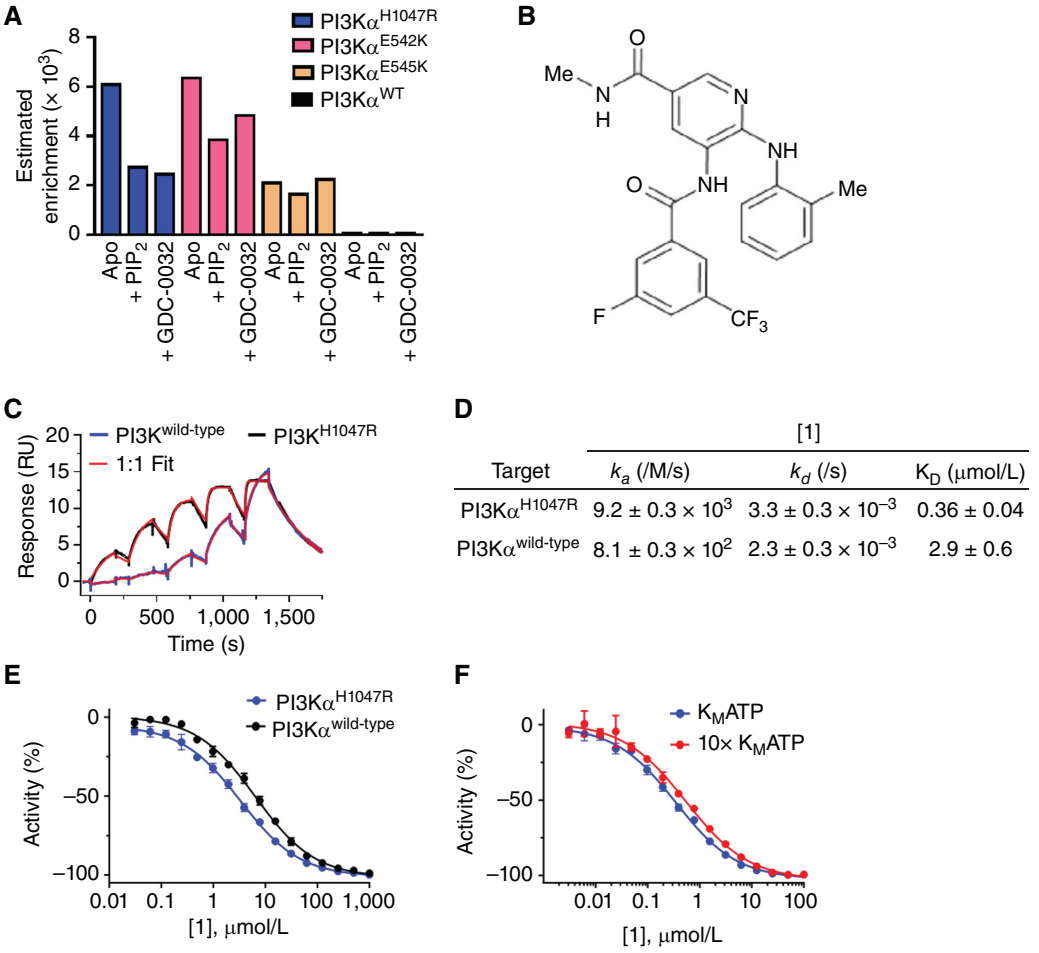

Figure 2. Discovery of an allosteric PI3Kα H1047R-selective inhibitor. **A,** Families of candidate binders that were enriched in the presence of PI3Kα H1047R protein relative to wild-type and not competitive with orthosteric ligands were prioritized for hit validation. **B,** Chemical structure of compound [1], which met DNA-encoded library (DEL) hit selection and validation criteria. **C,** Surface plasmon resonance (SPR) binding measurements of [1] toward PI3Kα H1047R and PI3Kα wild-type at 25°C. Increasing concentrations of [1] were injected onto protein immobilized onto the SPR surface using amine coupling. SPR sensograms (blue, wild-type; black, H1047R) were fit to one-step binding and dissociation equations (red) to determine the association rate (k_a), dissociation rate (k_d), and equilibrium dissociation constant (K_D) values shown in **D**. **E,** [1] inhibited the enzymatic activity of full-length recombinant PI3Kα H1047R and PI3Kα wild-type. **F,** Inhibition of PI3Kα H1047R by [1] was not competitive with ATP.

with the original X-ray structure (12) that membrane interactions are increased in H1047R. In addition to the positive charge of R1047 and the disengaged tail promoting activation through increased membrane interactions, the mutant kinase also samples a broader conformational ensemble in the HRD motif and activation loop of the kinase domain. This ensemble is consistent with a more active enzyme, suggesting that a strategy to restore the allosteric network could offer mutant selectivity. Due to the perturbation of regulatory contacts between the activation loop and the p85α regulatory subunit, such a strategy could also extend beyond inhibiting H1047R to other mutations, such as E542K and E545K, that likely also impact the conformational equilibrium governing p85α inhibition of p110α.

Mutant-Selective Small Molecules Identified by a DNA-Encoded Library Screen

To leverage the conformational differences along the allosteric network between PI3Kα WT and H1047R for mutant-selective inhibitor discovery, we performed a DNA-encoded library (DEL) selection. This screening campaign leveraged three key strengths to identify a mutant-selective allosteric inhibitor. First, we used full-length constructs that had been validated by CryoEM analysis. Second, we blocked the orthosteric site with an inhibitor to increase the chances of finding allosteric hits. Third, we focused on compounds that had differential enrichment for H1047R, E542K, and E545K over WT PI3Kα (Fig. 2A). Candidate hits were subsequently synthesized off-DNA and evaluated for inhibition and binding, which led to the identification of [1] (Fig. 2B).

To determine if [1] was selective for mutant PI3Kα over WT, we measured binding affinities by surface plasmon resonance. Consistent with its enrichment profile from the DEL screen, [1] bound 8-fold tighter to H1047R (K_D 360 ± 40 nmol/L) than to WT (K_D 2900 ± 600 nmol/L; Fig. 2C). This binding selectivity can be primarily attributed to a ~10-fold faster association rate (k_a) for the mutant (9.2 ± 0.3 × 10^3 per M/s) than for WT (8.1 ± 0.3 × 10^2 per M/s; Fig. 2D). The on-rate–driven selectivity

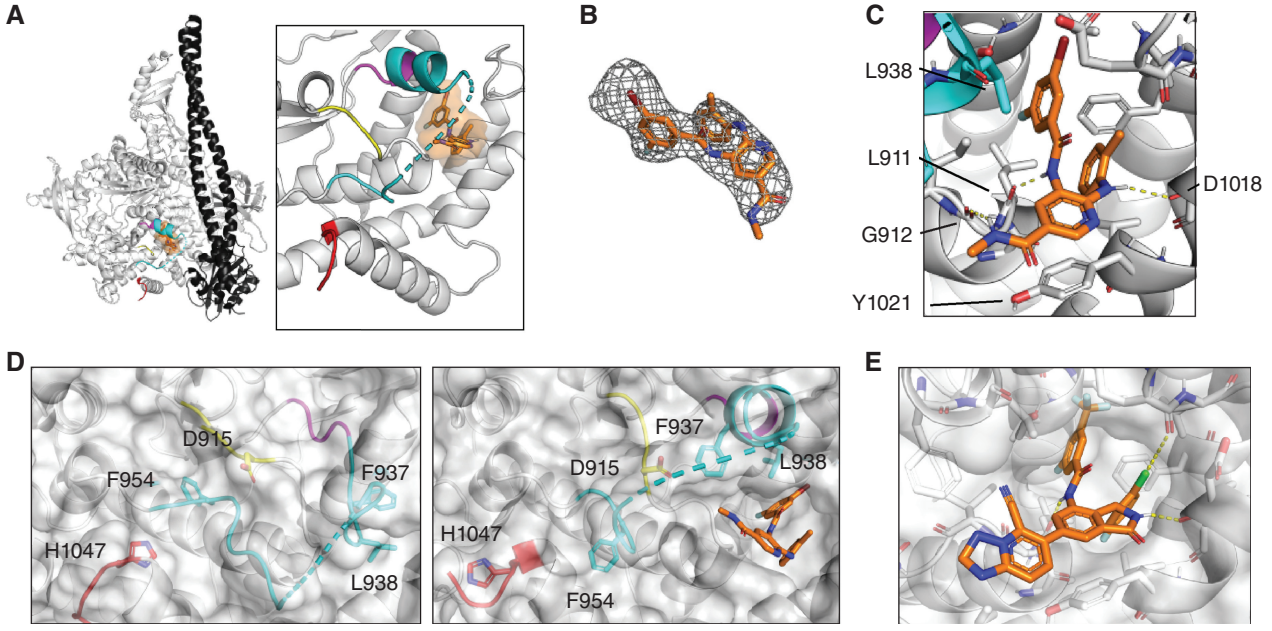

Figure 3. Discovery of an allosteric, mutant-selective binding site on PI3Kα. **A,** [2]-bound structure of PI3Kα H1047R, with [2] in orange, and allosteric network colored as in Fig. 1C. (inset) FO-FC omit map and anomalous dispersion map for [2]. **B,** Fo-Fc omit map of [2] extracted from PI3Kα H1047R-bound structure. **C,** Detailed view of [2] interaction with the binding site. **D,** Comparison of apo PI3Kα wild-type (left) and [2]-bound PI3Kα wild-type (right), with residues relevant to the binding-induced conformation rearrangement and allosteric communication depicted as sticks. **E,** Detailed view of RLY-2608 interaction with the binding site.

is unusual and suggests an origin in a conformational rearrangement that is favored in the mutant enzyme relative to WT.

Next, we determined whether the binding of [1] to PI3Kα inhibited the catalytic activity of the enzyme. We measured ADP product formation as the enzyme phosphorylated the substrate analogue diC8-PIP_2 (19). We found that [1] had a ~2-fold selectivity for PI3Kα H1047R (IC_{50} 334 ± 21 nmol/L) over WT (IC_{50} 647 ± 32 nmol/L; Fig. 2E). Moreover, the inhibition of PI3Kα H1047R by [1] was not ATP competitive (Fig. 2F), consistent with an allosteric mechanism of inhibition. Collectively, this identified an inhibitor with promising initial biochemical selectivity, resulting from altered association kinetics, and an allosteric mechanism of inhibition.

X-ray Crystallography Identifies the Origin of a Mutant-Selective Cryptic Pocket

To identify the interaction site of the PI3Kα H1047R-selective hit, we solved a 2.38 Å X-ray structure of tail-truncated PI3Kα WT bound to [2], a brominated analogue of our initial hit [1] (Fig. 3A). Notably, [2] (Supplementary Fig. S3A) presented a similar potency and selectivity profile to [1] against recombinant PI3Kα enzymes (Supplementary Fig. S3B–S3D), and the high-density signal of the bromine atom allowed the compound binding site and pose to be determined unambiguously (Fig. 3B). This structure revealed that the F,Br-phenyl and tolyl moieties of [2] displace the hydrophobic activation loop residues F937 and L938, binding to a cryptic pocket formed by p110α residues L812, L911, I999, I1019, and I1022. Additional interactions are formed by the [2] pyridine core, which displaces the planar peptide bond between L938 and D939 to pi-stack with Y1021, and the amide groups on either side of the core, which form hydrogen bonds with the backbone carbonyls of residues L911 and G912 (Fig. 3C). The open state of the cryptic pocket stabilized by [2] displaces multiple elements of the allosteric network identified by our combined EM, X-ray, and MD studies (Fig. 1). First, the N-terminal region of the activation loop is displaced as a result of the cryptic binding pocket opening. This displacement explains the loss of catalytic activity due to perturbation of the ATP-coordinating DFG motif, putative catalytic base H936, and substrate-coordinating lysines. H936 and the substrate-coordinating lysine residues are stabilized in a helical structure by hydrophobic contacts between L938 and the F,Br-phenyl ring of the compound. Second, activation loop residue F937 reorients to displace D915 of the HRD motif down toward F954 and the remainder of the allosteric network. F954 is repositioned to occupy the portion of the C-lobe where the C-terminal tail, including residues H1047 and W1051, is docked in the apo structure (Fig. 3D).

These interactions provide a rationale for the selectivity of [1] for H1047R over WT: burial of the C-terminal tail in WT p110α kinase domain constrains the conformations of the F954, HRD motif, and F937 regions, stabilizing a ligand-inaccessible cryptic site conformation; in contrast, the H1047R mutation favors the disengaged state of the C-terminal tail and perturbed conformations of F954, the HRD motif, and F937, increasing sampling of a ligand-accessible cryptic site. To test this idea, we hypothesized that truncating the C-terminal tail of WT PI3Kα would mimic the binding behavior of the H1047R-mutant protein. Indeed, the binding kinetics (Supplementary Fig. S4A) and biochemical inhibition (Supplementary Fig. S4B) of compound [1] to tailless WT (p110α 1-1050) are similar to H1047, with an association rate that is 10-fold faster than what is observed for full-length WT (p110α 1-1068; Supplementary Fig. S4C). These results link the conformational dynamics of the tail to the selective binding of [1]

Table 1. Biochemical inhibition and selectivity of [1], [3], and RLY-2608.

Target	[1]	[3]	RLY-2608
PI3Kα^{WT} IC_{50} (nmol/L)	647 ± 32	69 ± 9	48 ± 17
PI3Kα^{H1047R} IC_{50} (nmol/L)	334 ± 21	16 ± 4	4 ± 0
Selectivity (H1047R/WT)	1.9	4.3	12

in a cryptic allosteric pocket. Moreover, these results emphasize that using full-length protein, validated here by cryoEM, was important for the DEL screen: the tailless constructs would not have demonstrated the differential enrichment that led to the identification of this allosteric chemical series.

Conformational Dynamics-Based Design Drives Selectivity for H1047R over WT and Other Isoforms

To improve the potency and PI3Kα H1047R selectivity of [1], we used free energy perturbation calculations and X-ray structures of compounds bound to WT and H1047R to identify analogues. We initially made modifications to the bisaminopyridine core and peripheral toluene and methylamide groups. Bisaminopyridine replacement with an aminoisoxindole core [3] (Supplementary Text) resulted in a 9× IC_{50} improvement for PI3Kα H1047R and a 2× improvement in H1047R selectivity (Table 1). Further replacement of the toluene and methylamide groups of [3] with 2-chloro-5-fluorophenyl and [1,2,4]triazolo[1,5-a]pyridine-5-carbonitrile groups, respectively, resulted in RLY-2608, which has additional improvement in potency against PI3Kα H1047R and further improvement in selectivity (Table 1). These affinity improvements of the aminoisoxindole core likely stem from more effective space filling of the pocket, including a more extensive interaction with Y1021, along with a stronger hydrogen bond to the backbone of D1018 (1.9 Å in [3] vs. 2.5 Å in [2]). The 5-fluoro substitution in the final compound, RLY-2608, likewise results in improved packing of the hydrophobic pocket in which the phenyl group sits, whereas the 2-chloro substitution introduces a halogen-bond with the backbone carbonyl of E1012 (Fig. 3E).

The energetic coupling of tail disengagement and cryptic pocket opening provides an explanation for why this series has selectivity for mutant PI3Kα over WT. In addition, sequence differences at the binding site can explain the selectivity over other PI3K isoforms. Notably, F937 is substituted for Ile in β and γ; I1022 is substituted for Leu in β and δ; and I910 is substituted for Leu in all other isoforms (β, γ, δ). These substitutions provide an additional selectivity handle, augmenting the fact that these isoforms are also tightly regulated by p85 subunits that disfavor cryptic pocket opening. In addition to being 12x selective for mutant over WT PI3Kα, RLY-2608 is highly selective over isoforms (Supplementary Fig. S5) and does not detectibly inhibit other kinases (Supplementary Table S1). Furthermore, we observe comparable levels of biochemical selectivity for the helical mutants, E542K and E545K, following preincubation with RLY-2608 (Supplementary Table S2). Also, notably, the pan-mutant selectivity profile of RLY-2608 was comparable whether using liposomes or the soluble lipid substrate dic8-PIP_2 (Supplementary Table S3). This newly developed allosteric inhibitor should be able to inhibit the oncogenic activity of mutant kinase while avoiding the negative signaling consequences that come with inhibiting WT and other isoforms.

RLY-2608 Is Active in Cells against Tail and Helical Domain Mutations

To assess the selectivity of RLY-2608, we utilized an isogenic MCF10A cell line model system, where the expression of a single mutant allele is responsible for signaling. Treatment with an orthosteric molecule inhibits phosphorylation of AKT, a downstream marker of PI3K activation, equally between the different cell lines. However, RLY-2608 preferentially modulates signaling in the mutant cell lines (Fig. 4A). Additionally, we observed mutant selectivity when

Figure 4. Allosteric inhibition of mutant PI3Kα inhibits signaling and proliferation and leads to tumor growth inhibition *in vivo* with reduced insulin levels. **A,** Hemizygous MCF10A cell lines harboring the indicated *PIK3CA* alleles were incubated with a compound in a dose-response assay for 2 hours, and phosphorylated AKT (pAKT) was measured via Homogeneous time resolved fluorescence (HTRF) (Perkins Elmer). **B,** Similar to **A**, an endogenously *PIK3CA*-mutant cancer cell line (T47D) and a WT cell line were treated with the compound and viability was measured by CTG. **C,** Nude female mice implanted subcutaneously with T47D cells were administered the compound orally when tumor volume reached 200 mm^3, and tumor volume was measured twice weekly via caliper. **D,** Waterfall plot of tumor volume changes at the end of the study in nude female mice, implanted subcutaneously with estrogen pellets (Innovative Research of America) prior to MCF7 cell implant, and treated with single agents or combination regimens as indicated. **E,** Waterfall plots at the end of the study in athymic nude mice implanted with estrogen pellets and indicated tumor fragments. Treatment with RLY-2608 single agent and in combination with fulvestrant. **F,** Serum insulin and C-peptide levels were measured by ELISA (Crystal Chem) at the indicated time points after 4 days of repeat dosing in T47D tumor-bearing animals.

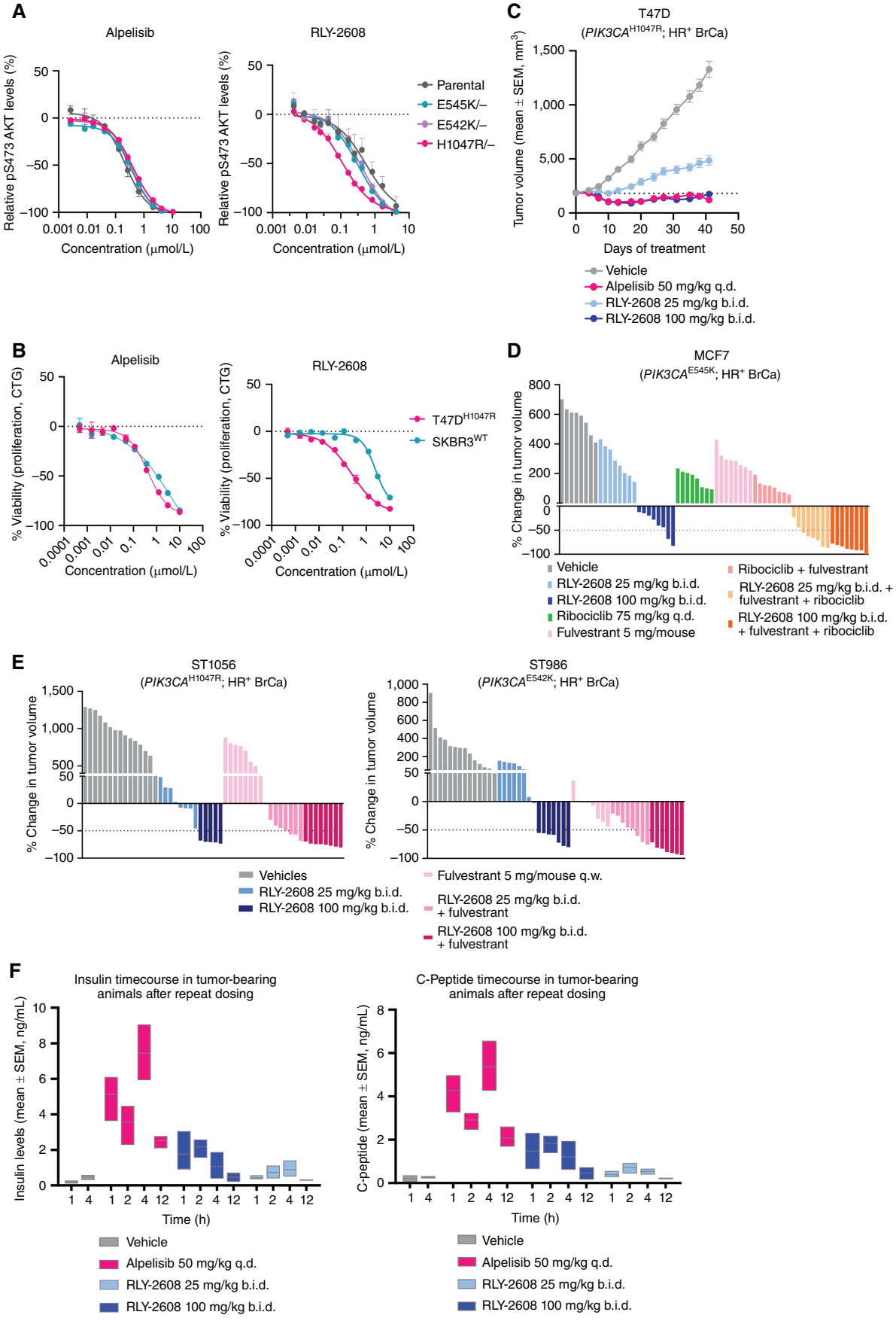

an endogenously mutant cancer cell line (T47D) was treated alongside a WT, but PI3K-dependent cell line (SKB3), whereas alpelisib equally inhibited both (Fig. 4B). These findings were extended to a panel of cancer cell lines, which harbor mutations spanning three hotspot residues in *PIK3CA* and represent various indications (Supplementary Fig. S6A and S6B). RLY-2608 led to inhibition of signaling and proliferation, which correlated with the inherent PI3Kα cellular dependency, as assessed by the activity of alpelisib, an orthosteric inhibitor. The ability of RLY-2608 to inhibit kinase domain and helical mutants across a variety of mutated *PIK3CA* cellular models suggests that these variants exhibit similar coupling between p85α dissociation and cryptic pocket opening.

RLY-2608 Inhibits Tumors in Animal Models with Reduced Impact on Insulin Levels

To assess the activity of RLY-2608 *in vivo*, we implanted mice with hormone receptor positive (HR^+) breast cancer cells (T47D) that are kinase domain mutant (H1047R; Fig. 4C). After tumor growth reached 200 mm^3, we orally administered the orthosteric inhibitor alpelisib or RLY-2608. In both models, RLY-2608 (100 mg/kg b.i.d.) led to significant tumor growth inhibition, resulting in stasis or regression similar to treatment with alpelisib. The activity of RLY-2608 was also assessed against HR^+ breast cancer cells (MCF7) that are helical domain mutant (E545K; Fig. 4D). Significant tumor regression was observed when mice were treated with RLY-2608 alone at 100 mg/kg. Tumor regression was further potentiated when RLY-2608 was combined with a clinically relevant dose of fulvestrant (estrogen receptor degrader) and in a triple combination with both fulvestrant and ribociclib (a cyclin-dependent kinase 4/6 inhibitor), clinical standard of care in this indication. Additionally, similar tumor regression was observed in $ER^+/HER2^-$ patient-derived xenografts, mutant in the kinase (ST1056: H1047R) or helical domain (ST986: E542K) using RLY-2608 alone at 100 mg/kg. Improved efficacy was also observed in combination with fulvestrant (Fig. 4E). Notably, these results indicate that RLY-2608 is active *in vivo* and can inhibit growth for tumors that are dependent on a variety of PI3Kα-activating mutations in a tolerated manner (Supplementary Fig. S7). Because a major complication for alpelisib observed clinically is dose-limiting hyperglycemia and hyperinsulinemia (17), we monitored insulin and insulin C-peptide levels as surrogate markers of glucose, which can be reliably measured in the tumor-bearing animals (Fig. 4F). Although alpelisib exhibited a substantial increase in both markers in the hours after treatment, even at the highest doses of RLY-2608 these markers remained lower than alpelisib treatment, with levels closer to baseline. Collectively, these studies indicate that RLY-2608 can maximally inhibit tumors driven by mutations impacting the regulation of PI3Kα while mitigating the hyperglycemia adverse effect that results from inhibiting WT protein.

Proof-of-Concept Clinical Activity

In the ongoing dose-escalation portion of the ReDiscover first-in-human study of RLY-2608 (NCT05216432), activity has been observed in patients with both *PIK3CA* kinase and helical domain mutant breast cancer without adverse events related to WT PI3Kα inhibition.

Case Study 1

Patient A is a 58-year-old female with metastatic (liver, lung, bone, LN) ER^+/PR^+, HER2 low breast cancer who progressed after 12 prior lines of therapy (endocrine, chemotherapy, and targeted therapy, including trastuzumab deruxtecan). Genomic analysis by tissue and circulating tumor DNA (ctDNA) showed activating *PIK3CA* H1047R and E453K mutations. The patient met enrollment eligibility criteria for the monotherapy arm of the study and was assigned to receive RLY-2608 400 mg p.o. b.i.d. Within 4 weeks of therapy, the patient had a marked improvement in bone pain. Furthermore, tumor marker evaluation at 4 weeks compared with baseline showed a reduction of CA15-3 (1598 to 933 U/mL) and CEA (68 to 24 U/mL). Radiographic evaluation after 8 weeks (C3D1) showed partial response with a decrease in multiple liver, lung, and soft-tissue target lesions [−36% in target lesions (TL) compared with baseline by RECIST 1.1]. Partial response was confirmed on subsequent scans with a maximum −48.8% change in TL compared with baseline (Fig. 5A). Consistent with mutant-selective PI3Kα targeting, little to no impact on glucose homeostasis (serum glucose, insulin, C-peptide; Fig. 5B), or skin reactions were observed. Treatment-emergent adverse events included dysuria, hypercalcemia, and abdominal pain. The patient had a continued response until clinical progression on study day 154.

Case Study 2

Clinical activity was also demonstrated in patients with helical mutations. Patient B is a 66-year-old female with metastatic (bone, soft tissue) $ER^+/PR^+/HER2^-$ breast cancer who progressed on standard of care with fulvestrant and palbociclib combination therapy. She was referred for clinical trial evaluation. Genomic analysis demonstrated a *PIK3CA* E542K mutation. The patient met enrollment eligibility criteria for the combination arm of the study and was assigned to receive RLY-2608 600 mg p.o. b.i.d. plus fulvestrant. Tumor marker evaluation at 4 weeks compared with baseline showed a reduction of CA15-3 (192 to 119 U/mL) and CEA (22 to 12 U/mL). Radiographic evaluation after 8 weeks (C3D1) showed partial response with disappearance of the soft-tissue target lesion (−100% in TL compared with baseline by RECIST 1.1). Radiographic response was confirmed with an additional evaluation at 12 weeks (Fig. 6A). Of note, PET/CT evaluation showed resolution of diffuse intense marrow uptake seen on the baseline scans. However, there were a few persistent intensely avid osseous nontarget lesions. Consistent with mutant-selective PI3Kα targeting, no impact on glucose homeostasis (Fig. 6B) or skin reactions were observed. Treatment-emergent adverse events included hypokalemia, anemia, and intermittent transaminitis (thought to be disease-related). The patient's treatment is currently ongoing as of study day 141.

In summary, these patient cases provide proof of concept that RLY-2608 is a first-in-class isoform- and mutant-selective allosteric inhibitor of PI3Kα, which can induce clinical responses in monotherapy, or in combination with fulvestrant, in breast cancers bearing kinase or helical mutations, with minimal impact on glucose homeostasis.

DISCUSSION

PI3Kα is the most frequently mutated kinase in all cancers, with oncogenic mutations detected in about 14% of patients

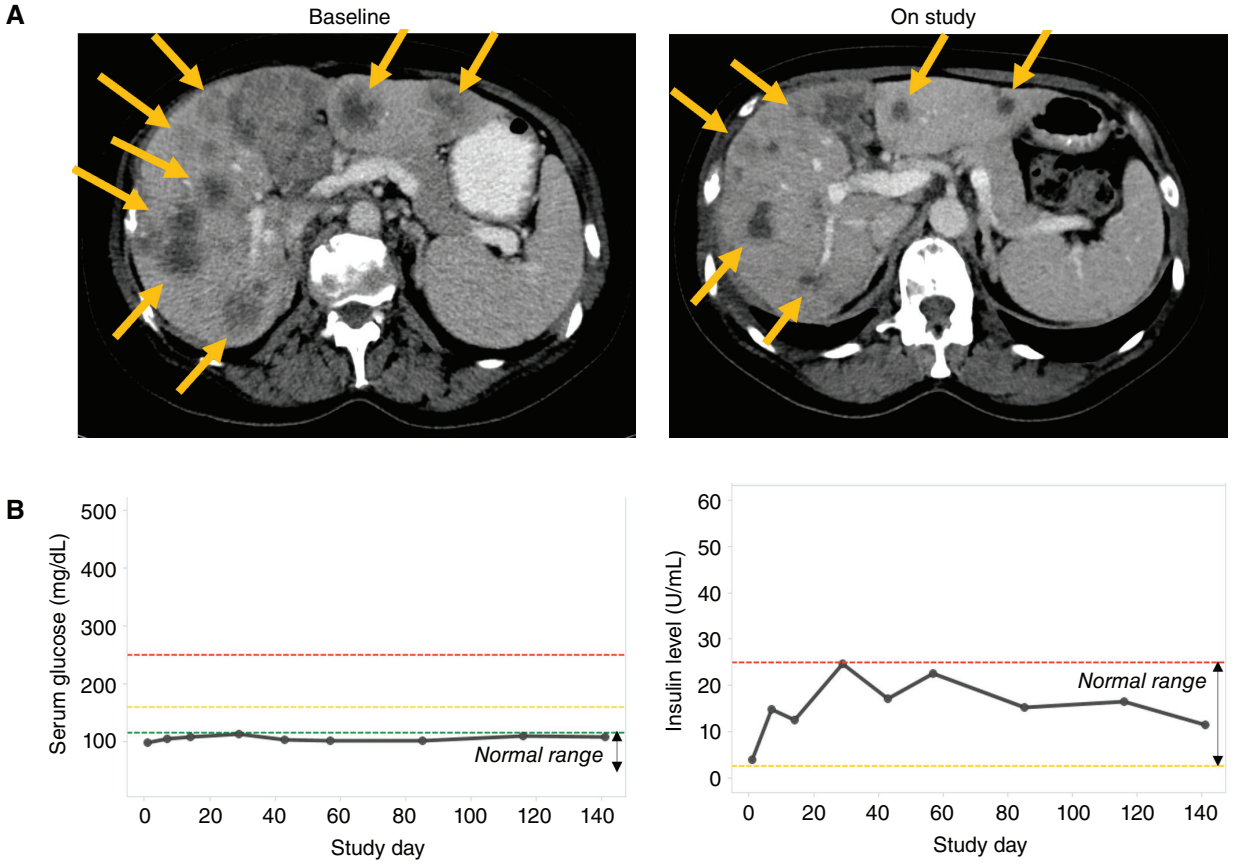

Figure 5. 58-year-old female with HR⁺ HER2 low metastatic breast cancer with *PIK3CA* H1047R and E453K mutations. **A,** Axial CT scan of the patient's abdomen, including areas of tumor in the liver (arrows), at baseline during screening, and after 8 weeks of therapy with a partial response per RECIST 1.1. **B,** Serum glucose and insulin levels during study treatment.

with solid tumors. Historically, the development of PI3Kα inhibitors has focused on the orthosteric site; however, the therapeutic effect of these agents is limited by a narrow therapeutic index due to on-target toxicity. Alpelisib is the only approved PI3Kα inhibitor and is indicated for the treatment of patients with advanced HR-positive *PIK3CA*-mutant breast cancer in combination with fulvestrant. However, approximately half of patients receiving alpelisib undergo dose reduction or treatment discontinuation due to severe toxicity related to WT PI3Kα inhibition such as hyperglycemia, diarrhea, and skin rash. These toxicities have made orthosteric inhibitors challenging to use in practice (20, 21), with intensive glucose monitoring and antidiabetic management limiting broader clinical adoption, and have made some potential combinations intolerable, such as with the CDK4/6 inhibitor ribociclib (22).

To overcome these liabilities, we have discovered compounds targeting a cryptic pocket by leveraging cryoEM, MD simulations, and a DEL screen. The resulting compound, RLY-2608, is a potent allosteric inhibitor with mutant and isoform selectivity *in vitro*, in cells, and animal models. We assessed the activity of this mutant-selective, allosteric inhibitor in preclinical models that allowed the interrogation of glucose homeostasis and tumor growth in the same animal. In line with what has been observed in patients, treatment with orthosteric inhibitors leads to increased insulin (10), a reflection of perturbed glucose homeostasis. In contrast, RLY-2608 caused significant tumor growth inhibition in xenografts harboring kinase and helical domain mutations with minimal impact on insulin levels, indicative of selective pan-mutant activity. Mutant selectivity may enable higher target engagement and wider therapeutic index in the clinic allowing for targeting solid tumors that may require higher suppression of PI3K pathway such as head and neck and gynecologic malignancies.

This wider therapeutic index of an allosteric inhibitor will also benefit patients on combination therapies. For example, in HR⁺ HER2⁻ breast cancer, doublet combinations with endocrine therapy with PI3Kα or CDK4/6 inhibitors have benefited patients. Although triplet combinations have the potential to further delay resistance and maximize clinical benefit for patients (23) with promise in preclinical studies, overlapping and additive toxicity has limited the tolerability of triplet combinations with orthosteric *PIK3CA* inhibitors with CDK4/6 inhibitors in the clinic (22). Our studies in breast cancer xenografts demonstrate that RLY-2608–based combination therapies with fulvestrant and ribociclib are well tolerated and more efficacious compared with single agent and fulvestrant–ribociclib combination.

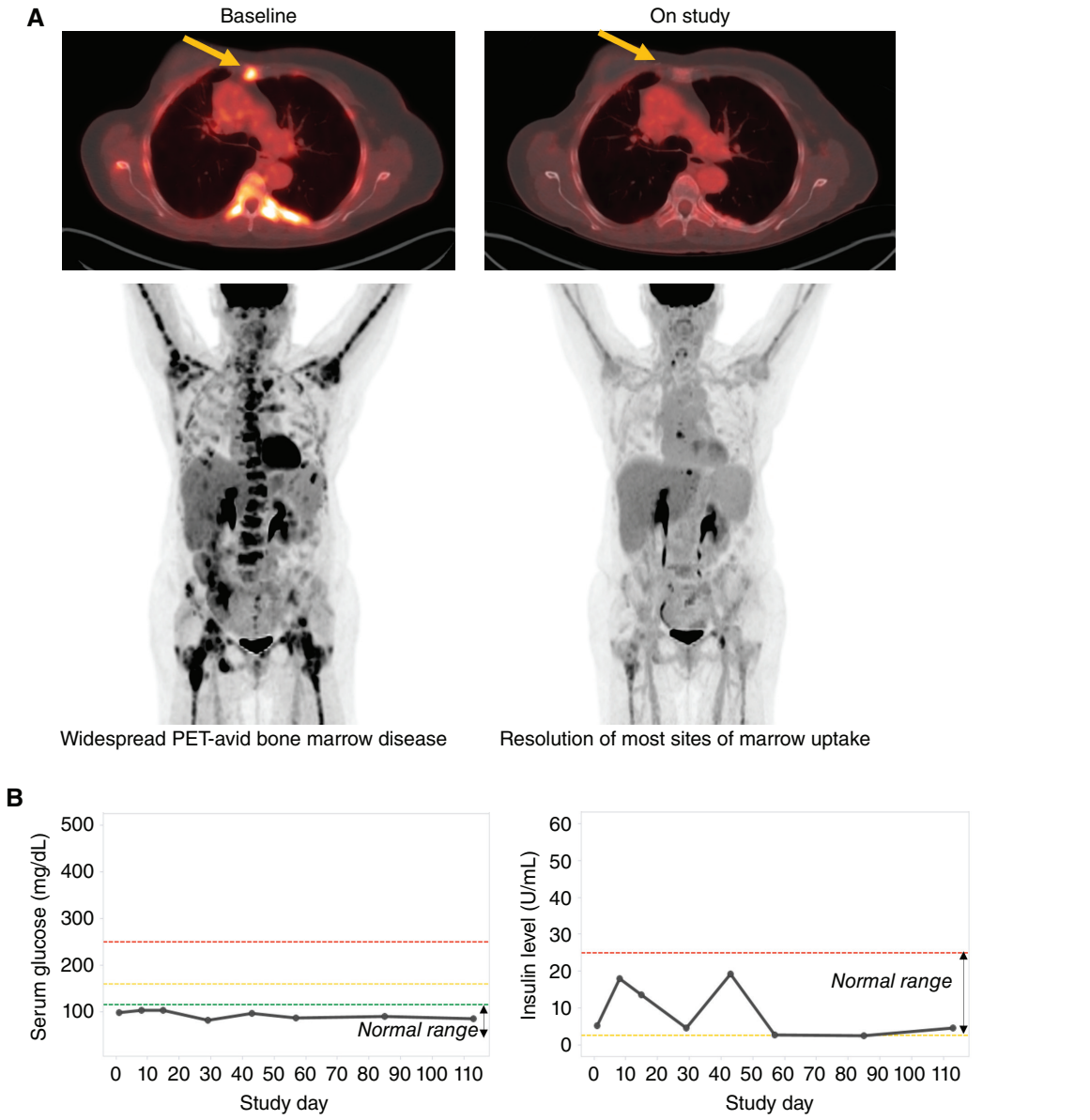

Figure 6. 66-year-old female with HR$^+$ HER2$^-$ metastatic breast cancer and *PIK3CA* E542K mutation. **A,** Partial response with disappearance of the soft-tissue target lesion (–100% in TL compared with baseline by RECIST 1.1). PET/CT evaluation showed resolution of diffuse intense marrow uptake seen on the baseline scans. **B,** Little to no impact on glucose homeostasis (serum glucose, insulin).

The two patient vignettes described here demonstrate clinical proof of concept in metastatic HR$^+$ HER2$^-$ breast cancer and the potential to have improved tolerability and efficacy with pan-mutant- and isoform-selective PI3Kα inhibition with the allosteric inhibitor RLY-2608. These two examples highlight patients who achieved confirmed responses with RLY-2608 treatment without adverse events that are associated with WT PI3Kα inhibition. These examples also demonstrate activity in a variety of contexts: in kinase and helical mutations, in earlier and later lines of therapy, and in monotherapy and combination with fulvestrant.

Two decades after the discovery of oncogenic *PIK3CA* mutations, our collective understating of optimal PI3Kα targeting continues to evolve. Allosteric mutant-selective agents provide a novel advantage of a broader therapeutic index over older generation PI3Kα inhibitors. To this end, the past few years have seen intensifying research activities in developing mutant-selective PI3Kα inhibitors (24, 25). RLY-2608 is a first-in-class PI3Kα inhibitor that demonstrates mutant-selective efficacy in the clinic. These features have the potential to improve outcomes in patients with *PIK3CA*-mutant tumors, in monotherapy, and in combination with other targeted therapies. The ongoing phase I/II ReDiscover trial (NCT05216432), studying RLY-2608 in monotherapy, in doublet with fulvestrant, and in triplet with CDK4/6 inhibitor and fulvestrant, will further define the potential benefit of RLY-2608 in patients with advanced *PIK3CA*-mutant solid tumors and breast cancer.

More broadly, the problem of isoform and mutant selectivity is common across many targets in oncology. Here, we have developed an approach to overcoming this problem via allosteric, rather than orthosteric, inhibitor discovery. In our study, it was essential to use cryoEM and molecular dynamics to discover differences in the conformational dynamics of mutant and WT. Next, we identified inhibitors that impinge on the discovered allosteric network using a DEL screen. Importantly, the conditions of the DEL screen must be biased to magnify the differences between mutant and WT protein. In our case, blocking the orthosteric site was essential to avoid molecules that target the active site, and using full-length protein was essential because the tail plays a key role in the equilibrium governing cryptic pocket opening. Due to the favorable properties of allosteric inhibitors for gaining specificity, we expect the integrated use of cryoEM, MD, and DEL screening that we have leveraged here can help attack many other important targets in the future.

METHODS

Protein Production

Expression of the Full-Length p110α/p85α Complex. The sequence for the untagged p110α; subunit is: MPPRPSSGELWGIHLMPPRI LVECLLPNGMIVTLECLREATLITIKHELFKEARKYPLHQLL QDESSYIFVSVTQEAEREEFFDETRRLCDLRLFQPFLKVIEPVG NREEKILNREIGFAIGMPVCEFDMVKDPEVQDFRRNILNVCKEA VDLRDLNSPHSRAMYVYPPNVESSPELPKHIYNKLDKGQIIVVI WVIVSPNNDKQKYTLKINHDCVPEQVIAEAIRKKTRSMLLSSEQ LKLCVLEYQGKYILKVCGCDEYFLEKYPLSQYKYIRSCIMLGRM PNLMLMAKESLYSQLPMDCFTMPSYSRRISTATPYMNGETSTKSL WVINSALRIKILCATYVNVNIRDIDKIYVRTGIYHGGEPLCDNVN TQRVPCSNPRWNEWLNYDIYIPDLPRAARLCLSICSVKGRKGA KEEHCPLAWGNINLFDYTDTLVSGKMALNLWPVPHGLEDLLNPI GVTGSNPNKETPCLELEFDWFSSVVKFPDMSVIEEHANWSVSRE AGFSYSHAGLSNRLARDNELRENDKEQLKAISTRDPLSEITEQE KDFLWSHRHYCVTIPEILPKLLLSVKWNSRDEVAQMYCLVKDWP PIKPEQAMELLDCNYPDPMVRGFAVRCLEKYLTDDKLSQYLIQ LVQVLKYEQYLDNLLVRFLLKKALTNQRIGHFFFWHLKSEMHNK TVSQRFGLLLESYCRACGMYLKHLNRQVEAMEKLINLTDILKQ EKKDETQKVQMKFLVEQMRRPDFMDALQGFLSPLNPAHQLG NLRLEECRIMSSAKRPLWLNWENPDIMSELLFQNNEIIFKNG DDLRQDMLTLQIIRIMENIWQNQGLDLRMLPYGCLSIGDCVGL IEVVRNSHTIMQIQCKGGLKGALQFNSHTLHQWLKDKNKGEI YDAAIDLFTRSCAGYCVATFILGIGDRHNSNIMVKDDGQLFHI DFGHFLDHKKKKFGYKRERVPFVLTQDFLIVISKGAQECTKT REFERFQEMCYKAYLAIRQHANLFINLFSMMLGSGMPELQSFDD IAYIRKTLALDKTEQEALEYFMKQMNDAHHGGWTTKMDWIF HTIKQHALN

The sequence for the c-terminal His-tag p85α subunit is: MHHHH HHHHGSLEVLFQGPSAEGYQYRALYDYKKEREEDIDLHLGD ILTVNKGSLVALGFSDGQEARPEEIGWLNGYNETTGERGDFPGT YVEYIGRKKISPPTPKPRPPRPLPVAPGSSKTEADVEQQALT LPDLAEQFAPPDIAPPLLIKLVEAIEKKGLECSTLYRTQSSSNLAELR QLLDCDTPSVDLEMIDVHVLADAFKRYLLDLPNPVIPAAVYSE MISLAPEVQSSEEYIQLLKKLIRSPSIPHQYWLTLQYLLKH FFKLSQTSSKNLLNARVLSEIFSPMLFRFSAASSDNTENL IKVIEILISTEWNERQPAPALPPKPPKPTTVANNGMNNNMSLQ DAEWYWGDISREEVNEKLRDTADGTFLVRDASTKMHGDYTLT LRKGGNNKLIKIFHRDGKYGFSDPLTFSSVVELINHYRNESLA QYNPKLDVKLLYPVSKYQQDQVVKEDNIEAVGKKLHEYNTQFQ EKSREYDRLYEEYTRTSQEIQMKRTAIEAFNETIKIFEEQCQ TQERYSKEYIEKFKREGNEKEIQRIMHNYDKLKSRISEIIDSRR RLEEDLKKQAAEYREIDKRMNSIKPDLIQLRKTRDQYLMWLTQ KGVRQKKLNEWLGNENTEDQYSLVEDDEDLPHHDEKTWNVG SSNRNKAENLLRGKRDGTFLVRESSKQGCYACSVVVDGEVKHC VINKTATGYGFAEPYNLYSSLKELVLHYQHTSLVQHNDSLNVT LAYPVYAQQRR

The affinity tag is underlined. All plasmids were generated following the standard protocol.

Purification of Wild-Type Full-Length p110α/p85α. Cell pellets from Expi 293F cells were resuspended in lysis buffer (50 mmol/L sodium phosphate, pH = 8.0, 400 mmol/L NaCl, 5% glycerol, 1% Triton X-100, 5 mmol/L 2-mercaptoethanol, 1 mmol/L sodium orthovanadate, Dnase, and 1 tablet of complete EDTA-free protease inhibitor) and lysed by three passes through a microfluidizer. The lysate was clarified by centrifugation at 30,000× *g* for 45 minutes. The clarified lysate was passed through a 5-mL equilibrated Protino Ni-NTA at 4°C. The immobilized material on the column was washed with 10 column volumes (CV) of buffer A (50 mmol/L Tris (pH 7.5), 300 mmol/L NaCl, 0.1 mmol/L EGTA, 0.1% β-ME, 0.03% Brij-35, 270 mmol/L Sucrose.) and then eluted by a 20 CV gradient of buffer A to buffer B (50 mmol/L Tris (pH 7.5), 300 mmol/L NaCl, 0.1 mmol/L EGTA, 0.1% β-ME, 0.03% Brij-35, 270 mmol/L Sucrose with 500 mmol/L imidazole). Fractions were analyzed by SDS-PAGE, and those containing heterodimer were gel filtered using a Superose 6 increase 10/300 GL equilibrated in 50 mmol/L Tris-HCl (pH 7.5), 300 mmol/L NaCl, 0.1 mmol/L EGTA, 0.03% Brij-35, 270 mmol/L sucrose, 0.1% β-ME. The prominent peak contained dimer and that material was then diluted and purified by Mono Q anion exchange chromatography column [eluted by a linear gradient from buffer A (50 mmol/L Tris-HCl (pH = 8.5), 1 mmol/L DTT) to buffer B (50 mmol/L Tris pH = 8.5, 500 mmol/L NaCl, 1 mmol/L DTT)]. The protein was concentrated and purified a final time by size-exclusion chromatography using a Superdex 200 GL 10/300 Increase equilibrated in storage buffer (20 mmol/L HEPES 7.6; 100 mmol/L NaCl; 5 mmol/L DTT, 1% glycerol).

Expression and Purification of p110α/p85α Fusion Constructs. Recombinant, human WT and H1047R PI3Kα were expressed in baculovirus-infected SF21 cells as fusions consisting of residues 318–615 of p85α and residues 1–1050, 1–1053, or 1–1068 of p110α. In each construct, a GSGSGG-linker separated an N-terminal HIS10 tag from the recognition sequence of 3C protease, and a GSPGISGGGGG-linker connected p85- and p110-derived sequences. To purify the proteins, cells were lysed under high pressure in a buffer containing 50 mmol/L sodium phosphate (pH 8.0), 400 mmol/L NaCl, 5% glycerol, 1% Triton X100, 1 mmol/L BME and cOmplete, EDTA-free Protease Inhibitor Cocktail (Sigma-Aldrich) and then centrifuged at 18,000 RPM for 60 minutes at 4°C. The proteins were enriched from the clarified lysates on Protino Ni-NTA Agarose (Macherey Nagel) using Affinity-Buffer A (50 mmol/L Sodium phosphate pH 8.0, 400 mmol/L NaCl, 1 mmol/L BME, 5% glycerol, 0.03% CHAPS) for washing and Affinity-Buffer B (50 mmol/L Sodium phosphate pH 8.0, 400 mmol/L NaCl, 1 mmol/L BME, 5% glycerol, 0.03% CHAPS, 500 mmol/L imidazole) for elution. Fractions containing the protein of interest were combined, desalted into 50 mmol/L Tris (pH 8.5), 1 mmol/L TCEP, 50 mmol/L NaCl, 5% glycerol, 0.03% CHAPS, and purified by ion exchange chromatography on a Mono Q 10/100 GL column (Cytiva). The protein was eluted from the column with a linear salt gradient, concentrated, and subjected to size-exclusion chromatography on a Superdex 200 Increase 10/300 GL column equilibrated in 20 mmol/L Tris-HCl (pH 8.0), 1 mmol/L TCEP, 150 mmol/L NaCl. Protein samples were concentrated to ~3 mg/mL for SPR or to ~13 mg/mL for crystallography and stored at −80°C subsequent to snap freezing in liquid nitrogen. For instances when the HIS10 tag was not required for immobilization, the protein was digested overnight at 4°C with HIS-tagged 3C protease between the above-described Ni-NTA and IEC steps, followed by a second Ni-NTA step for the removal of the tag, uncleaved protein, and 3C protease.

CryoEM Sample Preparation and Data Collection. 3 μL of 0.35 mg/mL PI3Kα heterodimer was applied to a glow discharged UltraAuFoil gold 1.2/1.3 300 mesh grid (Quantifoil Micro Tools) and plunge frozen using a Vitrobot Mark IV (Thermo Fisher). When used as a surfactant, a final concentration of 0.02% cetyltrimethylammonium bromide (CTAB) was added to the sample immediately before grid application. The surfactant was necessary to overcome the strong preferred particle orientation. Grids were imaged on a Titan Krios microscope operated at 300 kV and a nominal magnification of 105,000×, resulting in a calibrated pixel size of 0.819 Å/pixel, equipped with a 20 eV energy filter and a Gatan K3 direct detector. 2,058 movies were recorded for the nonsurfactant grids in super-resolution counting mode at 15 e^-/pix/s for a total of 2.68 seconds for a total dose of 60 $e^-/Å^2$ with a defocus range of −1 to −2.5 mm. The grids prepared with surfactant were imaged on the same microscope with the same settings, and a total of 6866 movies were recorded.

CryoEM Data Processing. Data processing was carried out in cryoSPARC v3.3.1 (26). A total of 4,284 movies from the $CTAB^+$ data set and 1,162 movies from the nonadditive data set were aligned and dose-weighted using cryoSPARC's Patch Motion Correction, and the contrast transfer function (CTF) parameters were determined using Patch CTF estimation. Particle picking was carried out by templated picking using templates produced from a refined and classified subset of particles using a particle diameter of 140 Å. 5,230,127 particles from the $CTAB^+$ data set and 804,237 particles from the nonsurfactant data set were boxed and downsampled to 1.7 Å/pixel. Particles from each data set were separately processed, and for each stack iterative rounds of reference-free two-dimensional (2D) classification were carried out to remove obvious mispicks. After 2D classification, particles from each data set were combined, and an initial volume was generated using ab intio reconstruction. Rounds of heterogeneous refinement and nonuniform refinement were further carried out to discard damaged or non-PI3Kα particles. The resulting particles were reextracted using an unbinned box size of 288 pixels. Local CTF estimation and nonuniform refinement improved alignment to a general and the final volume consisted of a total of 358,240 particles (306,741 particles from the $CTAB^+$ condition and 51,499 particles from the nonsurfactant condition).

Molecular Dynamics Simulations Methods

General Simulation Setup and Parameterization. Proteins and ions were parameterized with the Amber99SB*-ILDN force field (ref. 27; which builds on other modifications (28, 29) to Amber99 (30)]. The small molecules were parameterized using the general Amber force field (GAFF; ref. 31), with improved torsional parameters for rotatable bonds. The systems were solvated with water parameterized with the TIP3P water model (32) and neutralized with 150 mmol/L NaCl. The systems each contained ~247,000 atoms in a 140 × 140 × 140 Å cubic box.

Initial equilibration of the systems was performed on GPU Desmond (33) using a mixed NVT/NPT schedule (34). The systems were then further equilibrated by performing brief simulations on Anton (35), a specialized machine for molecular dynamics simulations; Anton was also used for all production simulations, which were initiated from the last frame of the Anton equilibration simulations. Production simulations were performed in the NPT ensemble at 310 K using the Martyna-Tobias-Klein barostat (36) and the Nosé-Hoover thermostat (37). The simulation time step was 2.5 fs, using a modified r-RESPA integrator (38) and evaluating long-range electrostatics every three time steps. Bond lengths to hydrogen atoms were constrained using an implementation (39) of M-SHAKE (40), and electrostatic forces were calculated using the *u*-series method. (41) A 9-Å cutoff was applied for the van der Waals calculations.

System Preparation. The apo p85/p110 complexes of the WT and the H1047R variant were prepared from PDB entries 4JPS (42) and 3HHM (12), respectively. The complexes were prepared for simulation using the Protein Preparation Wizard in Schrödinger Maestro. The C- and N-peptide termini were capped with amide and acetyl groups, respectively.

Simulation Analysis. *Tail dynamics*: The average root-mean-square deviation (RMSD) values were calculated for the heavy atoms of the tail (residues 1047–1061) of the p110 subunit using the last frame of the equilibration simulation and instantaneous structures from the trajectories, aligned on the entire p110 subunit.

Residue F954 and D915 dynamics: The average RMSD values were calculated for the heavy atoms of F954 and D915 of the p110 subunit using the last frame of the equilibration simulation and instantaneous structures from the trajectories, aligned on the entire p110 subunit.

Protein Crystallization and Structure Determination

Crystallography. All PI3Kα proteins were crystallized under identical conditions. Protein (13 mg/mL) was mixed in 1:10 ratio with Hampton Research additive screen mix Silver Bullet 22 (0.25% w/v p-coumaric acid, 0.25% w/v phenylurea, 0.25% w/v poly(3-hydroxybutyric acid), 0.25% w/v sulfaguanidine, 0.02 M HEPES sodium pH 6.8, HR2-996-22). For cocrystalization, compounds were added at a 10:1 ratio to protein. Crystals grew overnight at 20°C in sitting-drop vapor diffusion in a 1:1 solution of protein with 0.1 M HEPES pH 7.5 and 9% PEG-3350. Crystal growth was facilitated using seeds from prior protein crystals. Crystals were harvested at 20°C and flash frozen in liquid nitrogen after adding a cryoprotectant solution containing 0.1 M HEPES pH 7.5, 9% PEG-3350, and sequentially increasing concentrations of xylitol, to a final concentration of 30%.

Structure Determination. All crystallographic data were collected at 100 K at the following wavelengths WT 1–1053 apo: 0.979 Å, WT 1–1053 + [**2**]: 1.000 Å, H1047R 1–1053 apo: 1.033 Å, H1047R 1–1053 + [**1**]: 1.116 Å, H1047R 1–1053 + [**2**]: 1.116 Å, H1047R 1–1053 + [**3**]: 1.033 Å, WT 1–1053 + RLY-2608: 1.116 Å. Data were indexed, integrated, and scaled using autoPROC (Global Phasing). An initial structure was solved by molecular replacement using PDBID 2RD0 as a search model. Subsequent structures were solved by molecular replacement using structures presented herein. For all cases, the molecular replacement was performed using Phaser-MR (ref. 43; PMID: 17164524), as implemented in Phenix (ref. 43; PMID: 31588918). Final models were generated through iterative rounds of manual building in Coot (ref. 44; PMID: 15572765) and ISOLDE (ref. 45; PMID: 29872003) with refinement using phenix.refine. The CryoEM model, starting from the WT 1–1053 X-ray structure presented herein, was likewise generated through iterative manual refinement in Coot and ISOLDE and real-space refinement with Phenix.

Refinement Information. Ramachandran, sidechain, and clashscore statistics were as follows. (Molprobity) WT 1–1053 apo: 96.6% favored, 3.2% allowed, 0.16% outliers, 0.86% rotamer outliers, All-atom clashscore: 1.87. WT 1–1053 + [**2**]: 96.1% favored, 3.8% allowed, 0.1% outliers, 1.3% rotamer outliers, All-atom clashscore: 1.43. WT 1–1053 + RLY-2608: 95.4% favored, 4.66% allowed, 0% outliers, 0.94% rotamer outliers, All-atom clashscore: 1.85. H1047R 1–1053 apo: 96.6% favored, 3.2% allowed, 0.2% outliers, 0.95% rotamer outliers, All-atom clashscore: 2.08. H1047R 1–1053 + [**1**]: 97.0% favored, 2.9% allowed, 0.1% outliers, 1.36% rotamer outliers, All-atom clashscore: 1.38. H1047R 1–1053 + [**2**]: 96.0% favored, 4.0% allowed, 0% outliers, 1.02% rotamer outliers, All-atom clashscore: 1.56. H1047R 1–1053 + [**3**]: 95.6% favored, 4.3% allowed, 0% outliers, 1.79% rotamer outliers, All-atom clashscore: 1.66.

DNA-Encoded Library Selection and Enrichment Scoring. Full-length PI3Kα (WT, H1047R, E542K, and E545K) bearing N-terminal 8xHis tags were immobilized using Ni-NTA agarose in all selections. Data analysis and enrichment values were obtained as previously described (46).

Surface Plasmon Resonance Spectroscopy. Surface plasmon resonance experiments were performed on a Biacore S200 instrument (Cytiva Lifesciences) at 25°C using analysis buffer compromised of 20 mmol/L HEPES pH 7.5, 150 mmol/L NaCl, 0.005% Tween20 (v/v), 1 mmol/L $MgCl_2$, 1 mmol/L TCEP and 2% (v/v) DMSO. CM5 chips were preconditioned with 2 ×6 seconds pulses of 100 mmol/L HCl, 50 mmol/L NaOH, and 0.5% (v/v) SDS at flow of 100 μL/minutes. Approximately 6,000 response units (RU) of PI3Kα were immobilized onto the biosensor surface using amine coupling chemistry. Immobilization steps at a flow of 10 μL/minute: 7 minutes 400 mmol/L 1-ethyl-3-(3-dimethylaminopropyl) carbodiimide hydrochloride/100 mmol/L N-hydroxysuccinimide activation, 1–2 minutes 20 μg/mL PI3Kα in 10 mmol/L MES pH 6.0 with 0.03% CHAPS, 7 minutes 1 M ethanolamine HCl, pH 8.5. Using single-cycle kinetics compound was injected over the PI3Kα surface at increasing concentrations (top concentration 20 μmol/L, 3-fold dilution series, 5 concentrations) at a flow rate of 50 μL/minute. The association was set to 180 seconds followed by 4-minute dissociation. The raw data were processed using Biacore S200 Evaluation Software v1.1 (Cytiva Lifesciences), and the data were fitted kinetically to a 1:1 binding model that included a mass transfer limitation. Binding measurements were conducted 2 times to calculate a standard deviation.

PI3Kα Enzyme Activity and Inhibition Assays. To 1536-well plates (Corning 3937) containing the appropriate volume of 10 mmol/L inhibitor in DMSO dispensed from a 384-well low dead-volume (LabCyte LP-0200) plate using an Echo555, 2 nmol/L enzyme in assay buffer (50 mmol/L HEPES pH 7.4, 50 mmol/L NaCl, 6 mmol/L $MgCl_2$, 5 mmol/L DTT, and 0.03% CHAPS in distilled water) was added and allowed to incubate with inhibitors for 2 hours at room temperature. Next, a substrate solution containing 20 μmol/L PI(4,5)P_2 diC8 (Echelon Biosciences, Inc., P-4508) and 200 μmol/L ATP in substrate buffer (50 mmol/L HEPES pH 7.4, 50 mmol/L NaCl, 5 mmol/L DTT, and 0.03% CHAPS in distilled water) was added 1:1 to the enzyme solution, and PIP_2 phosphorylation was allowed to proceed for 1 hour at room temperature. The resulting ADP product concentration was then measured using the ADP-Glo Kinase Assay (Promega Corporation, V9103), according to the manufacturer's instructions, with luminescence quantified using an Envision plate reader (PerkinElmer 2104-0010) with a 0.1 second ultrasensitive luminescence protocol. Luminescence values were normalized, per-plate, to neutral and full-inhibition controls using the following equation:

$$\text{Normalized \% Inhibition} = (m_- - x)/(m_- - m_+) \times 100\%$$

where x is the luminescence value of the sample well, m_- is the mean luminescence value of the neutral control wells (DMSO vehicle in assay buffer), and m_+ is the mean luminescence value of the inhibitor control wells (GDC-0032 at a concentration of 100 nmol/L). Lastly, normalized concentration-response data were fit to a sigmoidal (four-parameter logistic) linear regression equation using GraphPad Prism to calculate inhibitor IC_{50} values.

Liposome Preparation and PI3Kα Inhibition Measurements. The following three lipids, 18:1 (Δ9-Cis) PE (DOPE, Avanti 850725), 18:1 PS (DOPS, Avanti 840035), and 18:1 PI(4,5)P_2 (PIP_2, Avanti 850155), were combined in a 75:23:2 molar ratio, and liposomes with a diameter of 100 nm were prepared via physical extrusion according to manufacturer recommendations. Liposome size and polydispersity were measured by dynamic light scattering on a Zetasizer (Malvern Panalytical). PI3Kα enzyme inhibition was measured using ADP-Glo, as described previously, with the PIP_2 substrate substituted with a liposome solution that contained PIP_2 at a concentration of 25 μmol/L in the enzyme reaction.

In Vitro *Cell Work*

Cell Culture. The mutant hemizygous lines were engineered in the immortalized, insulin growth factor-responsive breast epithelial cell line, MCF10A heterozygous background (Horizon Discovery, HD 101-011, HD 101-002). Cell line generation was performed by targeting the *PIK3CA* locus via nonhomologous end joining repair of Cas9 nuclease mediated double-strand DNA breaks in one targeting round resulting in a 2 bp deletion in exon 9 of transcript *PIK3CA*-201 (ENST00000263967.4) leading to a premature stop codon of the WT allele (Horizon Discovery) as verified by analysis of cDNA and gDNA.

T47D, NCIH1048, SKBR3, MCF7, ME180, MCF7 (ATCC), EFM19, CAL33, CAL51 (DSMZ), GP2D, OAW42, MFE280 (Sigma), and OVISE (JCRB Cell Bank) were purchased from commercial vendors. Cell lines were authenticated by short-tandem repeat DNA profiling by the cell line bank from which they were obtained or by IDEXX BioAnalytics (ICC13-7). They were all provided after testing Mycoplasma-free and were routinely tested while in culture. All cell lines were cultured for less than 1-month post-thaw and used within 10 passages from receipt. Cell lines were cultured at 37°C in 5% CO_2 humidified air, in media recommended by the vendor.

Pharmacodynamic Assay. Cells were seeded in 12 μL of media in a 384-well plate (PerkinElmer). After 24 hours of incubation at 37°C, 5% CO_2, cells were treated with DMSO or test compound in an additional 12.5 nL for 2 hours at 37°C, 5% CO_2. Phospho AKT (Ser473) cellular HTRF (CisBio; 64AKSPEY) assay was carried out per the manufacturer's instructions. Data were fit to a sigmoidal four-parameter curve (4PL; GraphPad Prism, RRID:SCR_002798) to determine IC_{50}.

Proliferation. Cells were seeded in 40 μL media into a 384-well, clear-bottom plate, including a day 0 untreated plate to be read after 24 hours. After 24 hours of incubation at 37°C, 5% CO_2, cells were treated with DMSO or test compound in additional 40 nL for 120 hours at 37°C, 5% CO_2. Following incubation, plates and CellTiter-Glo 2.0 (Promega) were equilibrated to room temperature for 30 minutes. 30 μL CellTiter-Glo 2.0 was added to all wells. Plates were placed on shaker (protected from light) at room temperature for 30 minutes and read on an EnVision plate reader. Data were normalized by subtracting day 0 values from all treated sample measurements followed by normalization to DMSO controls and conversion to percent viability. A sigmoidal four-parameter curve (4PL; GraphPad Prism, RRID:SCR_002798) was used to determine the IC_{50}.

Xenograft Studies. All procedures relating to animal handling, care, and treatment were approved by the Institutional Animal Care and Use Committee (IACUC) of the companies performing the studies and followed the guidance of the Association for Assessment and Accreditation of Laboratory Animal Care (AAALAC). Cell line–derived xenograft studies were conducted at Pharmaron, Inc. Female Balb/c nude mice at 6–8 weeks of age were inoculated subcutaneously on the flank with 2×10^7 T47D or 1.5×10^7 MCF cells in 0.1 mL of 1:1 mixture of 1640 RPMI: BD Matrigel. For MCF7-inoculated animals, a 17-beta Estradiol tablet (0.5 mg, 90-day release, Innovative Research of America) was implanted subcutaneously in the left flank. Patient-derived xenograft studies were conducted at START. Tumor fragments (~70 mg) were implanted subcutaneously in athymic nude mice. Animals were supplemented with exogenous estradiol ad libitum via drinking water throughout the study duration. Treatment was initiated when tumors reached a volume of about 200 mm^3. Tumors were measured twice weekly in two dimensions using a

caliper. Tumor volume was expressed in mm^3 using the formula: $V = 0.5\ a \times b2$, where a and b are the long and short diameters of the tumor, respectively.

ELISA. Serum samples were collected after repeat dosing (96 hours after treatment initiation) and analyzed per the manufacturer's protocol (Crystal Chem; Ultra-Sensitive mouse insulin kit 90082 and Mouse C-peptide kit 90050).

ReDiscover Phase I/II Study

ReDiscover is a global, open-label, phase I/II, first-in-human study (NCT05216432) of RLY-2608 in advanced cancer patients. Key objectives of phase I are to define the maximum tolerated dose and recommended phase II dose in monotherapy and in combination with fulvestrant, as well as the safety profile, pharmacokinetics, pharmacodynamics, and preliminary antitumor activity in patients with *PIK3CA* mutations and unresectable or metastatic solid tumors (monotherapy) or metastatic breast cancer (combination).

The key objectives of phase II are to define the overall response rate and duration of response per RECIST 1.1 for patients with advanced *PIK3CA* mutated solid tumors (monotherapy) or breast cancer (combination). Additional phase II objectives are to assess the safety, pharmacokinetics, and pharmacodynamics of RLY-2608 at the RP2D. The study was initiated in December 2021 and phase I dose escalation is ongoing concurrently with phase II dose expansion at the first selected RP2D of RLY-2608 600 mg b.i.d. with fulvestrant. The presented data herein are preliminary; the data cutoff was September 5, 2023.

The study was conducted in accordance with the Declaration of Helsinki and was reviewed and approved by the institutional review board of each clinical site. Written informed consent was obtained from all patients before study entry. Patients eligible for study participation were ≥18 years old; had Eastern Cooperative Oncology Group performance status 0–1; no prior treatment with PI3Kα inhibitors; no type 1 or 2 diabetes; no uncontrolled CNS metastases and adequate cardiac function. Additional enrollment criteria are provided in Supplementary Appendix S1. RLY-2608 was administered orally, twice daily, in 4-week cycles. Adverse events were graded per Common Terminology Criteria for Adverse Events (CTCAE) 5.0. The response was evaluated per RECIST version 1.1. Levels of ctDNA in plasma were assessed by next-generation sequencing, using 74-gene Guardant360 CDx (Guardant Health).

Accession Codes

The following data sets have been deposited in the Protein Data Bank (PDB):

CryoEM data for WT apo: 8TU6; H1047R X-ray structure: 8TS8; WT X-ray structure: 8TS7; WT X-ray structure bound to [2]: 8TSB; H1047R X-ray structure bound to [2]: 8TSA; H1047R X-ray structure bound to [1]: 8TS9; X-ray structure bound to [3]: 8TSC; WT X-ray structure bound to RLY-2608: 8TSD.

Data Sharing Statement

Further information and requests for access to data and/or reagents should be made directly to datasharingrequest@relaytx.com

Authors' Disclosures

A. Varkaris reports an agreement with Relay Therapeutics and Beigene for the performance of clinical trials. A. Varkaris is the principal investigator of these studies. E. Pazolli reports personal fees from Relay Therapeutics during the conduct of the study and outside the submitted work. H. Gunaydin reports other support from Relay Therapeutics during the conduct of the study and outside the submitted work; in addition, H. Gunaydin has a patent for WO2021222556A1 issued. A.A. Boezio reports patents for WO2023081757 and WO2021222556 issued, was an employee of Relay Therapeutics during the discovery and is still a shareholder of Relay Therapeutics. L. DiPietro reports personal fees from Relay Therapeutics outside the submitted work; in addition, L. DiPietro has a patent for WO2021222556A1 pending. A. Frost reports Relay Therapeutics funded the early proof-of-concept structural biology aspects of this study using cryoEM as a sponsored research agreement with the group at UCSF and is a shareholder of Relay Therapeutics. F. Giordanetto reports patents for US App No. 17/921580 and US App No 18/208023 pending. E.P. Hamilton reports grants from Relay Therapeutics during the conduct of the study; grants from AbbVie, Acerta Pharma, ADC Therapeutics, AKESOBIO Australia, Amgen, Aravive, ArQule, Artios, Arvinas, AtlasMedx, BeiGene, Black Diamond, Bliss BioPharmaceuticals, Boehringer Ingelheim, Bristol Myers Squibb, Cascadian Therapeutics, Cullinan, Curis, CytomX, Dana-Farber Cancer Inst, Dantari, Deciphera, Duality Biologics, eFFECTOR wTherapeutics, Eisai, grants and other support from Ellipses Pharma, grants from Elucida Oncology, EMD Serono, Fochon Pharmaceuticals, FujiFilm, G1 Therapeutics, H3 Biomedicine, Harpoon, Hutchinson MediPharma, Immunogen, Immunomedics, Incyte, Infinity Pharmaceuticals, Inspirna, InvestisBio, Jacobio, Karyopharm, K-Group Beta, Kind Pharmaceuticals, Leap Therapeutics, Loxo Oncology, Lycera, Mabspace Biosciences, Macrogenics, MedImmune, Merus, Millennium, Molecular Templates, Myriad Genetic Laboratories, Nucana, OncoMed, Onconova Therapeutics, Oncothyreon, ORIC Pharmaceuticals, Orinove, PharmaMar, Pieris Pharmaceuticals, Pionyr Immunotherapeutics, Plexxikon, Prelude Therapeutics, Profound Bio, Radius Health, Regeneron, Relay Therapeutics, Repertoire Immune Medicine, Rgenix, SeaGen, Sermonix Pharmaceuticals, Shattuck Labs, Silverback Therapeutics, StemCentRx, Sutro, Syndax, Syros, Taiho, TapImmune, Tesaro, Tolmar, Torque Therapeutics, Treadwell Therapeutics, Verastem, Zenith Epigenetics, Zymeworks, grants and other support from Accutar Biotechnology, AstraZeneca, Daiichi Sankyo, Gilead Sciences, Lilly, Mersana, Novartis, Olema, from Orum Therapeutics, Pfizer, Roche/Genentech, Stemline Therapeutics, other support from Entos, Fosun Pharma, Greenwich LifeSciences, Jazz Pharmaceuticals, Medical Pharma Services, Theratechnologies, Tubulis, Verascity Science, and Zentalis Pharmaceuticals outside the submitted work. M. Holliday reports personal fees from Relay Therapeutics, Inc. during the conduct of the study. J.R. LaRochelle reports other support from Relay Therapeutics during the conduct of the study. A. Lescarbeau reports patents for WO2023081757 and WO2021222556 issued and is an employee and shareholder of Relay Therapeutics. B. Lormil reports a clinical research agreement with Relay Therapeutics for performing a phase I trial on RLY2608. M.M. Mader reports other support from Eli Lilly and Company, Pfizer, and Relay Therapeutics outside the submitted work; in addition, M.M. Mader has patents for WO 2023288242, WO 2021222556, and WO 2020231990 pending. B.G. Mar reports other support from Relay Therapeutics during the conduct of the study and other support from Blueprint Medicines outside the submitted work. T.H. McLean reports personal fees from Relay Therapeutics outside the submitted work; in addition, T.H. McLean has a patent for WO2021222556A1 pending. A.M. Schram reports personal fees and other support from Relay Therapeutics during the conduct of the study, other support from AstraZeneca, BeiGene/Springworks, Black Diamond Therapeutics, Elevation Oncology, Kura Oncology, LOXO/Lilly, Northern Biologics, Pfizer, PMV Pharma, Repare Therapeutics, Revolution Medicine, and Surface Oncology, personal fees and other support from Merus, and personal fees from Flagship Pioneering, Redona Therapeutics, Blueprint Bio, and Mersana outside the submitted work. K. Shortsleeves reports other support from employee and shareholder of Relay outside the submitted work; in addition, K. Shortsleeves has a patent for WO2021222556A1 pending. J. Wilbur reports personal fees from Relay Therapeutics outside the submitted work. B.R. Williams reports being a shareholder in Relay Therapeutics. H. Zeng reports being an employee and shareholder of Relay Therapeutics. W.P. Walters reports that he is a leader and employee with equity interest in Relay Therapeutics, Inc. D.E. Shaw is the sole

beneficial owner and chief scientist of D. E. Shaw Research, which has a multi-target collaboration and licensing agreement with Relay Therapeutics. By way of his ownership of D. E. Shaw Research, D.E. Shaw also has an indirect equity interest in Relay Therapeutics. D.E. Shaw Research collaborated with Relay Therapeutics in the development of the research results disclosed in the paper. D.A. Bergstrom is an executive officer and shareholder in Relay Therapeutics, Inc-. J. Watters reports personal fees from RADD Pharmaceuticals outside the submitted work. J.S. Fraser reports grants, personal fees, and other support from Relay Therapeutics during the conduct of the study and outside the submitted work. P.D. Fortin reports personal fees from Matchpoint Therapeutics and Decrypt Biomedicine outside the submitted work and is a leader and employee with an equity interest in Relay Therapeutics, Inc. D. R. Kipp is an employee and shareholder of Relay Therapeutics. No disclosures were reported by the other authors.

Authors' Contributions

A. Varkaris: Conceptualization, resources, data curation, formal analysis, supervision, validation, investigation, visualization, methodology, writing–original draft, project administration, writing–review and editing. **E. Pazolli:** Conceptualization, data curation, formal analysis, supervision, validation, investigation, visualization, methodology, writing–original draft, project administration, writing–review and editing. **H. Gunaydin:** Conceptualization, data curation, formal analysis, supervision, validation, investigation, visualization, methodology, writing–original draft, project administration, writing–review and editing. **Q. Wang:** Conceptualization, data curation, software, formal analysis, investigation, visualization, methodology, writing–original draft, writing–review and editing. **L. Pierce:** Conceptualization, data curation, software, investigation, visualization, methodology, writing–original draft, writing–review and editing. **A.A. Boezio:** Conceptualization, data curation, formal analysis, supervision, validation, investigation, visualization, methodology, project administration. **A. Bulku:** Data curation, formal analysis, validation, investigation, methodology. **L. DiPietro:** Data curation, formal analysis, validation, investigation, methodology. **C. Fridrich:** Data curation, formal analysis, validation, investigation, methodology. **A. Frost:** Conceptualization. **F. Giordanetto:** Resources, investigation, methodology, project administration. **E.P. Hamilton:** Conceptualization, data curation, formal analysis, supervision, validation, investigation, methodology, writing–review and editing. **K. Harris:** Conceptualization, resources, data curation, supervision, validation, investigation, visualization, methodology, project administration, writing–review and editing. **M. Holliday:** Conceptualization, data curation, formal analysis, validation, investigation, methodology, writing–original draft, writing–review and editing. **T.L. Hunter:** Data curation, investigation, visualization, methodology. **A. Iskandar:** Data curation, formal analysis, validation, investigation, methodology. **Y. Ji:** Data curation, investigation, methodology. **A. Larivée:** Data curation, formal analysis, validation, investigation, methodology. **J.R. LaRochelle:** Conceptualization, data curation, formal analysis, supervision, validation, investigation, visualization, methodology, writing–original draft, project administration, writing–review and editing. **A. Lescarbeau:** Data curation, formal analysis, validation, investigation, methodology. **F. Llambi:** Conceptualization, supervision, investigation, methodology. **B. Lormil:** Data curation, investigation, visualization, methodology. **M.M. Mader:** Conceptualization, supervision, investigation, project administration. **B.G. Mar:** Conceptualization, data curation, supervision, validation, investigation, visualization, methodology, writing–review and editing. **I. Martin:** Conceptualization, supervision, investigation, project administration. **T.H. McLean:** Conceptualization, data curation, methodology, project administration. **K. Michelsen:** Data curation, formal analysis, validation, investigation, visualization, methodology, writing–original draft. **Y. Pechersky:** Data curation, software, formal analysis, validation, investigation, methodology. **E. Puente-Poushnejad:** Conceptualization, data curation, formal analysis, supervision, validation, investigation, visualization, Methodology, project administration, writing–review and editing. **K. Raynor:** Data curation, formal analysis, validation, investigation, methodology. **D. Rogala:** Data curation, formal analysis, validation, investigation, methodology. **R. Samadani:** Data curation, Formal analysis, Investigation, Methodology, Project administration. **A.M. Schram:** Conceptualization, data curation, formal analysis, supervision, validation, investigation, visualization, methodology, project administration, writing–review and editing. **K. Shortsleeves:** Data curation, formal analysis, validation, investigation, visualization, methodology, writing–original draft, writing–review and editing. **S. Swaminathan:** Data curation, investigation, methodology, project administration. **S. Tajmir:** Data curation, investigation, visualization, methodology. **G. Tan:** Conceptualization, data curation, formal analysis, supervision, validation, investigation, visualization, methodology, writing–review and editing. **Y. Tang:** Conceptualization, data curation, formal analysis, validation, investigation, visualization, methodology, project administration. **R. Valverde:** Conceptualization, data curation, formal analysis, validation, investigation, visualization, methodology, writing–original draft. **B. Wehrenberg:** Conceptualization, data curation, formal analysis, validation, investigation, visualization, methodology, writing–original draft. **J. Wilbur:** Conceptualization, data curation, formal analysis, supervision, validation, investigation, visualization, methodology. **B.R. Williams:** Conceptualization, data curation, formal analysis, supervision, validation, investigation, visualization, methodology. **H. Zeng:** Conceptualization, data curation, formal analysis, supervision, validation, investigation, visualization, methodology, project administration. **H. Zhang:** Data curation, formal analysis, validation, investigation, methodology. **W.P. Walters:** Conceptualization, data curation, formal analysis, supervision, validation, methodology. **B.B. Wolf:** Conceptualization, data curation, formal analysis, supervision, validation, investigation, visualization, methodology, writing–review and editing. **D.E. Shaw:** Conceptualization, resources, supervision. **D.A. Bergstrom:** Conceptualization, resources, supervision, writing–review and editing. **J. Watters:** Conceptualization, resources, data curation, formal analysis, supervision, validation, investigation, visualization, methodology, writing–original draft, project administration, writing–review and editing. **J.S. Fraser:** Conceptualization, data curation, formal analysis, supervision, validation, investigation, visualization, methodology, writing–original draft, project administration, writing–review and editing. **P.D. Fortin:** Conceptualization, data curation, formal analysis, supervision, validation, investigation, visualization, methodology, writing–original draft, project administration, writing–review and editing. **D.R. Kipp:** Conceptualization, data curation, formal analysis, supervision, validation, investigation, visualization, methodology, writing–original draft, project administration, writing–review and editing.

Acknowledgments

The authors thank the patients, their families, and caregivers for their support of this research. This study was sponsored by Relay Therapeutics, Inc. A. Varkaris acknowledges support by Department of Defense Physician Research Award (PC200820) and American Society of Clinical Oncology (ASCO) (to A. Varkaris). A. Schram acknowledges support from the ASCO Conquer Cancer Foundation Career Development Award, National Cancer Institute P30CA008748 Cancer Clinical Investigator Team Leadership Award, Cycle for Survival, and Memorial Sloan Kettering Cancer Center Support Grant (P30 CA008748).

The publication costs of this article were defrayed in part by the payment of publication fees. Therefore, and solely to indicate this fact, this article is hereby marked "advertisement" in accordance with 18 USC section 1734.

Note

Supplementary data for this article are available at Cancer Discovery Online (http://cancerdiscovery.aacrjournals.org/).

Received August 16, 2023; revised October 21, 2023; accepted October 27, 2023; published first November 13, 2023.

REFERENCES

1. Whitman M, Downes CP, Keeler M, Keller T, Cantley L. Type I phosphatidylinositol kinase makes a novel inositol phospholipid, phosphatidylinositol-3-phosphate. Nature 1988;332:644–6.
2. Fruman DA, Chiu H, Hopkins BD, Bagrodia S, Cantley LC, Abraham RT. The PI3K pathway in human disease. Cell 2017;170:605–35.
3. Vanhaesebroeck B, Stephens L, Hawkins P. PI3K signalling: the path to discovery and understanding. Nat Rev Mol Cell Biol 2012;13:195–203.
4. Jenkins ML, Ranga-Prasad H, Parson MAH, Harris NJ, Rathinaswamy MK, Burke JE. Oncogenic mutations of PIK3CA lead to increased membrane recruitment driven by reorientation of the ABD, p85 and C-terminus. Nat Commun 2023;14:181.
5. Liu X, Yang S, Hart JR, Xu Y, Zou X, Zhang H, et al. Cryo-EM structures of PI3Kalpha reveal conformational changes during inhibition and activation. Proc Natl Acad Sci U S A 2021;118:e2109327118.
6. Burke JE, Perisic O, Masson GR, Vadas O, Williams RL. Oncogenic mutations mimic and enhance dynamic events in the natural activation of phosphoinositide 3-kinase p110alpha (PIK3CA). Proc Natl Acad Sci U S A 2012;109:15259–64.
7. Chakrabarti M, Gabelli SB, Amzel LM. Allosteric activation of PI3Kalpha results in dynamic access to catalytically competent conformations. Structure 2020;28:465–74.
8. Bailey MH, Tokheim C, Porta-Pardo E, Sengupta S, Bertrand D, Weerasinghe A, et al. Comprehensive characterization of cancer driver genes and mutations. Cell 2018;173:371–85.
9. Samuels Y, Wang Z, Bardelli A, Silliman N, Ptak J, Szabo S, et al. High frequency of mutations of the PIK3CA gene in human cancers. Science 2004;304:554.
10. Goncalves MD, Hopkins BD, Cantley LC. Phosphatidylinositol 3-kinase, growth disorders, and cancer. N Engl J Med 2018;379:2052–62.
11. Tankova T, Senkus E, Beloyartseva M, Borstnar S, Catrinoiu D, Frolova M, et al. Management strategies for hyperglycemia associated with the alpha-selective PI3K inhibitor alpelisib for the treatment of breast cancer. Cancers (Basel) 2022;14:1598.
12. Mandelker D, Gabelli SB, Schmidt-Kittler O, Zhu J, Cheong I, Huang CH, et al. A frequent kinase domain mutation that changes the interaction between PI3Kalpha and the membrane. Proc Natl Acad Sci U S A 2009;106:16996–7001.
13. Liu X, Zhou Q, Hart JR, Xu Y, Yang S, Yang D, et al. Cryo-EM structures of cancer-specific helical and kinase domain mutations of PI3Kalpha. Proc Natl Acad Sci U S A 2022;119:e2215621119.
14. Hart JR, Liu X, Pan C, Liang A, Ueno L, Xu Y, et al. Nanobodies and chemical cross-links advance the structural and functional analysis of PI3Kalpha. Proc Natl Acad Sci U S A 2022;119:e2210769119.
15. Baselga J, Im SA, Iwata H, Cortes J, De Laurentiis M, Jiang Z, et al. Buparlisib plus fulvestrant versus placebo plus fulvestrant in postmenopausal, hormone receptor-positive, HER2-negative, advanced breast cancer (BELLE-2): a randomised, double-blind, placebo-controlled, phase 3 trial. Lancet Oncol 2017;18:904–16.
16. Di Leo A, Johnston S, Lee KS, Ciruelos E, Lonning PE, Janni W, et al. Buparlisib plus fulvestrant in postmenopausal women with hormone-receptor-positive, HER2-negative, advanced breast cancer progressing on or after mTOR inhibition (BELLE-3): a randomised, double-blind, placebo-controlled, phase 3 trial. Lancet Oncol 2018;19:87–100.
17. Janku F, Yap TA, Meric-Bernstam F. Targeting the PI3K pathway in cancer: are we making headway? Nat Rev Clin Oncol 2018;15:273–91.
18. Andre F, Ciruelos E, Rubovszky G, Campone M, Loibl S, Rugo HS, et al. Alpelisib for PIK3CA-mutated, hormone receptor-positive advanced breast cancer. N Engl J Med 2019;380:1929–40.
19. Jia Y, Quinn CM, Kwak S, Talanian RV. Current in vitro kinase assay technologies: the quest for a universal format. Curr Drug Discov Technol 2008;5:59–69.
20. Shen S, Chen Y, Carpio A, Chang C, Iyengar NM. Incidence, risk factors, and management of alpelisib-associated hyperglycemia in metastatic breast cancer. Cancer 2023 doi 10.1002/cncr.34928.
21. Miller J, Armgardt E, Svoboda A. The efficacy and safety of alpelisib in breast cancer: a real-world analysis. J Oncol Pharm Pract 2022;28:1152–6.
22. Tolaney SM, Im YH, Calvo E, Lu YS, Hamilton E, Forero-Torres A, et al. Phase Ib study of ribociclib plus fulvestrant and ribociclib plus fulvestrant plus PI3K inhibitor (Alpelisib or Buparlisib) for HR(+) advanced breast cancer. Clin Cancer Res 2021;27:418–28.
23. Cortes J, Im SA, Holgado E, Perez-Garcia JM, Schmid P, Chavez-MacGregor M. The next era of treatment for hormone receptor-positive, HER2-negative advanced breast cancer: Triplet combination-based endocrine therapies. Cancer Treat Rev 2017;61:53–60.
24. Buckbinder L, St Jean DJ, Tieu T, Ladd B, Hilbert B, Wang W, et al. STX-478, a mutant-selective, allosteric PI3Ka inhibitor spares metabolic dysfunction and improves therapeutic response in PI3Ka-mutant xenografts. Cancer Discov 2023;13:2432–47.
25. Juric D, Jhaveri K, Beeram M, Hamilton E, Chau V, Hanley MP, et al. Abstract OT3-08-01: a phase 1 trial of LOXO-783, a potent, highly mutant-selective, brain-penetrant allosteric PI3Kα H1047R inhibitor in PIK3CA H1047R-mutant advanced breast cancer (aBC) and other solid tumors (PIKASSO-01, trial in progress). Cancer Res 83, 2023 (suppl. 5; abstr OT3-08-01).
26. Punjani A, Rubinstein JL, Fleet DJ, Brubaker MA. cryoSPARC: algorithms for rapid unsupervised cryo-EM structure determination. Nat Methods 2017;14:290–6.
27. Lindorff-Larsen K, Piana S, Palmo K, Maragakis P, Klepeis JL, Dror RO, et al. Improved side-chain torsion potentials for the Amber ff99SB protein force field. Proteins 2010;78:1950–8.
28. Best RB, Hummer G. Optimized molecular dynamics force fields applied to the helix-coil transition of polypeptides. J Phys Chem B 2009;113:9004–15.
29. Hornak V, Abel R, Okur A, Strockbine B, Roitberg A, Simmerling C. Comparison of multiple Amber force fields and development of improved protein backbone parameters. Proteins 2006;65:712–25.
30. Wang J, Cieplak P, Kollman PA. How well does a restrained electrostatic potential (RESP) model perform in calculating conformational energies of organic and biological molecules? J Comput Chem 2000;21:1049–74.
31. Wang J, Wolf RM, Caldwell JW, Kollman PA, Case DA. Development and testing of a general amber force field. J Comput Chem 2004;25:1157–74.
32. Jorgensen WL, Chandrasekhar J, Madura JD, Impey RW, Klein ML. Comparison of simple potential functions for simulating liquid water. J Chem Phys 1983;79:926–35.
33. Bergdorf M, Robinson-Mosher S, Guo X, Law K-H, Shaw DE. [cited 2021 March 22]. Available from: https://www.deshawresearch.com/publications/Desmond-GPU_Performance_April_2021.pdf.
34. Bowers KJ, Chow E, Xu H, Dror RO, Eastwood MP, Gregersen BA, et al. Scalable algorithms for molecular dynamics simulations on commodity clusters. Proceedings of the ACM/IEEE Conference on Supercomputing (SC06). Tampa, FL2006. p. 43.
35. Shaw DE, Grossman JP, Bank JA, Batson B, Butts JA, Chao JC, et al. Anton 2: Raising the bar for performance and programmability in a special-purpose molecular dynamics supercomputer. SC IEEE; 2014. p. 41–53.
36. Martyna GJ, Tobias DJ, Klein ML. Constant pressure molecular dynamics algorithms. J Chem Phys 1994;101:4177–89.
37. Hoover WG. Canonical dynamics: equilibrium phase-space distributions. Phys Rev A 1985;31:1695–7.
38. Predescu C, Lippert RA, Eastwood MP, Ierardi D, Xu H, Jensen MØ, et al. Computationally efficient molecular dynamics integrators with improved sampling accuracy. Mol Phys 2012;110:967–83.
39. Lippert RA, Bowers KJ, Dror RO, Eastwood MP, Gregersen BA, Klepeis JL, et al. A common, avoidable source of error in molecular dynamics integrators. J Chem Phys 2007;126:046101.

40. Kräutler V, van Gunsteren WF, Hünenberger PH. A fast SHAKE algorithm to solve distance constraint equations for small molecules in molecular dynamics simulations. J Comput Chem 2001;22:501–8.
41. Predescu C, Lerer AK, Lippert RA, Towles B, Grossman JP, Dirks RM., et al. The u-series: a separable decomposition for electrostatics computation with improved accuracy. J Chem Phys 2020;152:084113.
42. Furet P, Guagnano V, Fairhurst RA, Imbach-Weese P, Bruce I, Knapp M, et al. Discovery of NVP-BYL719 a potent and selective phosphatidylinositol-3 kinase alpha inhibitor selected for clinical evaluation. Bioorg Med Chem Lett 2013;23:3741–8.
43. Liebschner D, Afonine PV, Baker ML, Bunkoczi G, Chen VB, Croll TI, et al. Macromolecular structure determination using X-rays, neutrons and electrons: recent developments in Phenix. Acta Crystallogr D Struct Biol 2019;75(Pt 10):861–77.
44. Emsley P, Cowtan K. Coot: model-building tools for molecular graphics. Acta Crystallogr D Biol Crystallogr 2004;60(Pt 12 Pt 1): 2126–32.
45. Croll TI. ISOLDE: a physically realistic environment for model building into low-resolution electron-density maps. Acta Crystallogr D Struct Biol 2018;74(Pt 6):519–30.
46. Cuozzo JW, Centrella PA, Gikunju D, Habeshian S, Hupp CD, Keefe AD, et al. Discovery of a Potent BTK inhibitor with a novel binding mode by using parallel selections with a DNA-Encoded chemical library. ChemBioChem 2017;18:864–71.